NEAR-FIELD NANOPATTERNING AND ASSOCIATED ENERGY TRANSPORT ANALYSIS WITH THERMOREFLECTANCE

A Dissertation

by

ALOK SONI

Submitted to the Office of Graduate Studies of
Texas A&M University
in partial fulfillment of the requirements for the degree of

DOCTOR OF PHILOSOPHY

Chair of Committee,	Sy-Bor Wen
Committee Members,	C. Steve Suh
	Choongho Yu
	Chin Su
Head of Department,	Andreas A. Polycarpou

August 2013

Major Subject: Mechanical Engineering

ABSTRACT

Laser nano-patterning with near-field optical microscope (NSOM) and the associated energy transport analysis are achieved in this study. Based on combined experimental/theoretical analyses, it is found that laser nano-patterning with a NSOM probes strongly depend on the laser conditions and material properties of the target: the energy transport from the NSOM probes to the targets changes from pure optical to a combination of thermal and optical transport when the pulse duration of laser is increased from femtosecond to nanosecond. As a result, the mechanisms of nano-pattern formation on targets changes from nano-ablation to nano-oxidation/ recrystallization when the laser pulse duration is increased from femtosecond to nanosecond.

Also, with the laser nano-patterning experiments, thermal damage of NSOM probes is observed which can be attributed to the low transport efficiency (10^{-4} – 10^{-6}) and associated heating of the metal cladding of NSOM probes. The heating of NSOM probes are studied with developed time harmonic and transient thermoreflectance (TR) imaging. From time harmonic TR when the NSOM probes are driven with continuous laser, it is found that the location of heating of NSOM probes is ~20-30μm away from the NSOM tip. The strength of the heating is determined by the laser power (linear dependence), wavelength of the laser (stronger with short λ), and aperture size of NSOM probes (stronger when aperture size < $\lambda/2$). From the transient TR imaging when the NSOM probes are driven with pulsed laser, it is found that the peak temperature of the NSOM probe shifts much closer to the tip. The possible reason for the change in the

location of peak temperature when continuous laser is changed to pulsed laser can be attributed to the competition between the heat generation and dissipation rates at different location of the probe: the tip experiences highest temperature with pulsed heating as the entire heating processes is adiabatic. The tip also experiences highest heat dissipation rate due to its large surface-to-volume ratio which overcomes the heat generation at the tip under quasi-steady state resulting in shift of the hot spot. The knowledge obtained in this study can be important in the future design of more efficient NSOM probes and other nano-optic devices.

To my parents and my teachers

ACKNOWLEDGEMENTS

First and foremost, I would like to thank my committee chair, Dr. Sy-Bor Wen for his guidance and support throughout the course of this research. I would also like to thank my committee members, Dr. Steve Suh, Dr. Chin Su and Dr. Choongho Yu for their guidance and helpful discussions.

I would like to thank my colleagues Vijay Sundaram, Young Kyong Jo, Yu Yang and Chien-Fan Chen for their support in conducting my experiments and providing valuable suggestions.

I would like to acknowledge the facilities available at Texas A&M University, especially the Material Characterization Facility, Microscopy & Imaging center, Center for Nanoscale Science & Technology and Texas A&M supercomputing facilities which facilitated my research. Thanks also go to Dr. Richard Russo at Lawrence Berkeley National Lab for allowing us to use his lab facility; Dr. Xianglei Mao and Vasileia Zormpa at Lawrence Berkeley National Lab and Dr. Dave Diercks at the University of North Texas for their helpful discussions and support.

Finally, thanks to my parents, brother and sister for their encouragement and support.

TABLE OF CONTENTS

Page

LIST OF FIGURES

Page

Page

Page

LIST OF TABLES

1. INTRODUCTION

1.1 Lasers

Lasers (Light Amplification by Stimulated Emission of Radiation) are devices providing amplified coherent radiation at wavelengths from infrared to ultraviolet. A laser system typically composed with (i) an active medium to amplify electromagnetic radiation, (ii) a pumping process to excite the atoms (or molecules) present in the active medium into higher energy states and (iii) a resonator to store the coherent electromagnetic field and enable the field to interact with active medium for continued amplification [1, 2].

Laser light has distinct properties such as high spatial/temporal coherences, small divergence angle and high intensity, which are valuable in academic research (e.g., fluorescence microscopy, remote sensing, interferometry, laser diagnostics of combustion and laser velocimetry [3, 4]) and industrial applications (e.g., photolithography, laser machining and optical communications [5, 6]). Laser can operate either in a continuous (constant power over time) or pulsed mode (peak power for a short duration). Continuous wave (CW) lasers are commonly adopted in applications requiring low power and long exposure time, such as laser bar-code reader, laser printer, CD/DVD reader/writer, photolithography, fluorescence microscopy and laser projection displays. Pulsed lasers are mainly applied in applications requiring high intensity such as laser cutting, laser drilling and laser surgery, in which materials are removed from a target through different mechanisms (e.g. exfoliation, laser ablation). In addition to material

processing, pulsed lasers are also valuable in fast/ultrafast imaging owing to its controllable short pulse durations (from micro to atto seconds).

In traditional laser machining, laser beam is focused on a target with a lens. Absorption of the intense laser energy at a localized spot results in removal of surface material through either thermal (i.e., heating, melting and evaporation) or non-thermal processes (e.g., Coulomb explosion [7]). When the laser light is focused in the far field with the traditional reflective or refractive optics, the minimum achievable size of the laser spot (which is also the optical resolution of laser machining) is determined by diffraction. Even with the highest numerical aperture and aberration free lens, diffraction-limited minimum spot size is about half of the laser wavelength (~200 nm for visible light) in the far field.

With the advancement in nanotechnology, there is a great desire to further improve the optical resolution to the nano-scale (i.e., < 100 nm [8]) in order to bring the benefits of laser processing to the nano fields. Compared with the existing nano-fabrication techniques such as electron beam, x-rays, focused ion beam (FIB), laser based nano-fabrication can have benefits in lower cost owing to its ability to be conducted in a background gas, and fast processing speed owing to its high energy output.

1.2 Nano-optic Devices and Near Field Optical Microscope (NSOM)

Nano-optic devices are optical components which can confine light to a region $<\lambda/2$ [9, 10] compared with traditional diffractive and reflective lenses. Compared with far field propagating waves, in nano-optical devices, non-propagating electromagnetic

field which exists at the interface of two regions with different optical properties is utilized. This non-propagating electromagnetic field, which decays exponentially within a short distance (~ 10's nm) from the interface, is named as evanescent wave. The diffraction limit of evanescent waves can be much smaller (< $\lambda/2$) compared with the propagating light, and can resolve features in the nanoscale range [9-11]. Therefore, with nano-optical devices utilizing evanescent waves, traditional laser based machining have potential to be extended to the nanoscale.

The first nano-optical devices was conceptualized by Synge in 1928 [12]. Synge proposed that a tiny particle smaller than ~$\lambda/2$ can be brought very close to the sample (e.g. a biological cell) and then the scattered light from the tiny particle can be collected by an objective lens to achieve deep sub-wavelength resolution. He also suggested the use of a tiny hole in an opaque screen (or conical waveguide) that can be utilized as localized light source for achieving high resolution microscopy. Due to the fabrication difficulties, the consequent optical devices (i.e., near field scanning optical microscope (NSOM)) was not demonstrated until 1984 by Dieter W. Pohl [13]. As of now, NSOM is still the only commercialized nano-optic device provides optical resolution better than $\lambda/2$ for optical imaging and detections.

Typically, the NSOM system is composed with a deep sub-wavelength near-field light source at the tip of an NSOM probe and a nano-positioning and scanning system to bring this probe close to the surface of the target ($<<\lambda$ where the evanescent waves are strong). The NSOM system can have an apertureless or apertured probe to provide highly confined light source. In an apertured NSOM probe, a deep sub-wavelength near-

field light source can be provided through a deep sub-wavelength aperture at the end of tapered optical fiber. In the aperture configuration light is focused to a sub-diffraction region through multiple reflections within a tapered optical fiber with a metal cladding. At the tip of NSOM probe the sub-diffraction size (i.e. 50-150 nm) aperture does not allow the light to propagate further, instead creates a non- propagating localized near-field. In the apertureless configuration, a sharp tip (with radius $<<\lambda$) provides a confined non-propagating electric field when illuminated with far-field radiation.

When the deep sub-wavelength light source is brought closer to the target surface ($<<\lambda$) with the nano-positioning system of the NSOM, the photon energy transfers from the light source to the target through evanescent waves (i.e., photon tunneling from the quantum point of view). The induced optical singles from the target then can be detected in the far or near fields. With a x-y scanning of the NSOM probe on the target, the induced optical signal from the target can be reconstructed into 2D optical image which provides resolution better than $\sim\lambda/2$ and is determined by the feature size of the deep sub-wavelength light source from the tip of the NSOM probe. In addition to deep sub-wavelength optical microscopy, NSOM system is now commonly adopted in nanoscale tip enhanced Raman spectroscopy (TERS), fluorescence detection for chemical and bio studies. In most of these applications low power continuous laser is applied to construct the deep sub-wavelength light source from the tip of the NSOM probes.

1.3 Nano-machining with NSOM

Through increasing the light intensity applied to NSOM probes, there is a high potential to deliver intense laser light to a deep sub-wavelength region on the target. This

ultra-confined intense light on a target surface can be utilized in nano-machining, chemical and material characterization (e.g. laser induced breakdown spectroscopy), laser microsurgery, laser assisted chemical reaction (e.g,, laser based chemical vapor deposition (LCVD), dry- etching) and laser surface modification with high spatial resolution in a background gas environment.

Compared with far field laser ablations, high intensity light emitting from the NSOM probes cannot be achieved by simply increasing the input laser energy. Considering the light transport efficiency of NSOM probes are <0.01% and most of the laser energy is dissipated into heat around the tip of the NSOM probes, higher laser energy input can results in high temperature around the tip the probe especially in its metal cladding. The consequent thermal damage of NSOM probes can (e.g., melting and exfoliation of the metal cladding around the tip of the NSOM probes) cause malfunction of the NSOM system during the operation [14-23]. For most NSOM probes, the damage threshold of NSOM probes can be similar or even smaller than the required energy level for surface patterning of the targets (depends on the optical and thermal properties of target material) [24-26]. The limited range of the working laser fluence and the sensitivity of the nano-patterning with respect to the physical and chemical properties of target material can be the major challenges in applying NSOM probes in deep sub-wavelength nano-machining.

1.4 Energy Transport Analysis with Thermoreflectance Imaging

To determine the light induced heating in order to control the undesired side effects of heating during NSOM operation, especially under high light intensity, a

detailed study of the energy transport in NSOM probes based on experimental determination of the temperature evolution of NSOM probe during operation is required. Indirect temperature assessments of NSOM probes was carried out through measuring the thermal expansion of the probe and relate the expansion to the temperature field with a combined optics-energy transport analysis . Direct temperature measurement was also carried out with single point micro thermocouple [27] and thermoreflectance measurements [28] with. In the micro-thermocouple measurements, a temperature profile was obtained by measuring temperature at different locations along the tapered region of the NSOM probe. Temperature measurement with micro thermocouple provides the spatial resolution limited to a few microns (i.e., size of the thermocouple probe). In addition to the low spatial resolution, the thermal mass of the thermocouple affects the temperature measurement especially when the size of NSOM probe is comparable or smaller than the thermocouple. Single point thermoreflectance, on the other hand, provides a nonintrusive measurement, which is preferred. However, single point thermoreflectance measurement is time consuming for determining the entire temperature profile of the NSOM probe since the same measurement has to be carried out for a large number of positions along the NSOM probe.

The difficulties of single point thermoreflectance measurement in determining the temperature profile of NSOM probes during their energy transport can be alleviated with 2D thermoreflectance imaging when a single detector is replaced with a detecting array such as CCD (charge coupled device). The 2D thermoreflectance imaging allows a determination of the 2D temperature profile in a time efficient manner (i.e., from single

measurement). Since its first demonstration in 1997, 2D thermoreflectance imaging is adopted for determining the quasi-steady-state temperature distribution and the associated energy transport. Based on the above reasoning, 2D thermoreflectance imaging is identified to be an appropriate tool for non-intrusive temperature measurement of NSOM probes during operation and subsequent energy transport analysis.

1.5 Scope of the Dissertation

In Chapter 2, the concept of far-field optics, near-field optics and the classical diffraction limits are discussed. Based on the concept of near-field optics, working principle of near-field optical microscope (NSOM) system and its configuration is explained. After the introduction of NSOM, energy transport in NSOM systems and the associated heating issues in NSOM systems are discussed.

In chapter 3, the developed methodology and experimental setup for direct nano-patterning with NSOM systems are presented. Results from controlled experiments with different laser and target material conditions are listed. From the morphology of the nano-patterns from the experiments, possible mechanisms for nano-pattern generation on different targets under different laser conditions are proposed.

In chapter 4, nano-pattern formation on silicon with nano-second laser pulse under argon and air are specially studied. It is determined that the pattern formation mechanism under this special condition is mainly through melting and recrystallization.

In chapter 5, the development of thermoreflectance imaging method for temperature measurement of nano-optic devices (NSOM) under quasi-steady state

operation (e.g. cyclic heating under low frequency) is presented. The developed method is also used for direct and non-intrusive temperature measurement of NSOM probes under CW laser illumination.

In Chapter 6, a novel method for nanosecond time-domain thermoreflectance imaging is presented. Major challenges of thermoreflectance imaging with pulsed laser due to high coherence of the laser are described. Developed methods to overcome these obstacles are demonstrated. The results of nanosecond non-intrusive temperature measurement of a micro gold resistor and a NSOM probe with this new method under pulsed laser heating are also presented.

In chapter 7, a conclusion of the contributions of the present work along with the future applications is listed.

2. THEORY AND BACKGROUND

2.1 Classical Diffraction Limit

Deviation of light from rectilinear propagation (i.e. geometric optics) was first reported by Francesco Grimaldi in 1600s and he coined the word 'diffraction' to explain this remarkable behavior of light. In the 19th century, light diffraction was studied in more detail by Augustin-Jean Fresnel and later by Christiaan Hyugens and G. Kirchhoff. In a competition sponsored by French academy in 1818, Fresnel presented his theory of diffraction which became a strong support for the wave nature of light. The Fresnel's theory later advanced by Christiaan Hyugens is known as Hyugens-Fresnel principle. According to the Hyugens-Fresnel principle, when a wavefront of light is obstructed by an object, every unobstructed point of the wavefront, at a given instant of time, serves as a source of spherical secondary wavelets with the same frequency as of the primary wave. The amplitude and phase of the optical field at any point beyond is determined by the superposition of all these wavelets. The subsequent intensity distribution after the superposition of these wavelets is called a diffraction pattern [29]. Figure 2.1 illustrates the application of Hyugens-Fresnel principle to explain the diffraction of a plane wave obstructed by a screen with a circular aperture.

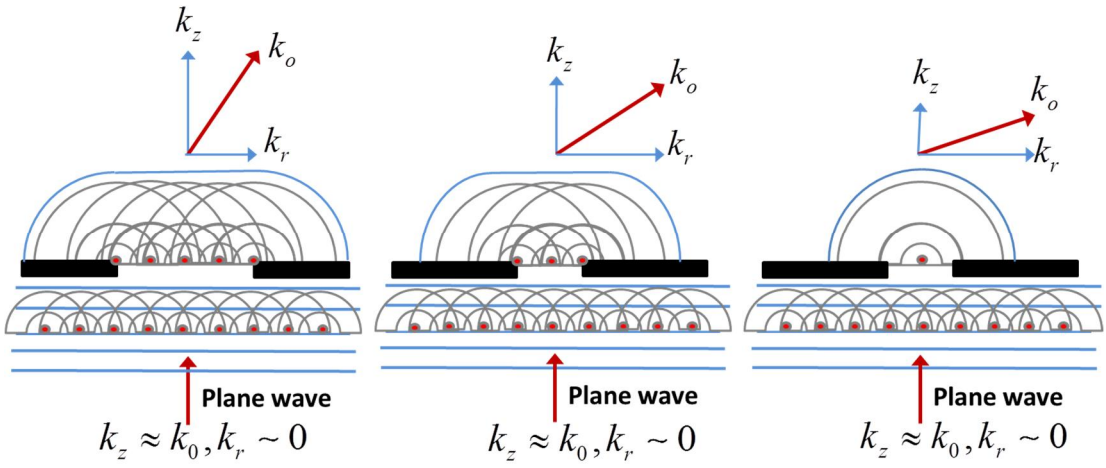

Figure 2.1: Diffraction through a circular aperture is illustrated using Hyugen-Fresnel principle; Effect of aperture size on spatial distribution of wave vectors in propagating (z-direction) and radial direction

The intensity distribution of the diffraction pattern on a screen at a distance '*R*' from a small circular aperture with radius '*a*' obtained from Hyugens-Fresnel principle is given by:

$$I(\theta) = I(0)\left[\frac{2J_1(kaq/R)}{kaq/R}\right]^2 \tag{1.1}$$

where J_1 is first order Bessel function, q denotes the radial distance on the image plane. This image shows an axially symmetric distribution, with a high irradiation central spot (known as Airy's disk) surrounded by alternating bright and dark rings (known as side lobes) of decreasing intensity from q=0. The radius of the Airy's disk can be obtained from the first zero of the Bessel function $J_1(x)=0$ when x=3.832 that is,

$$\frac{kaq_1}{R} = 3.83 \Rightarrow q_1 = 1.22\frac{R\lambda}{2a} \tag{1.2}$$

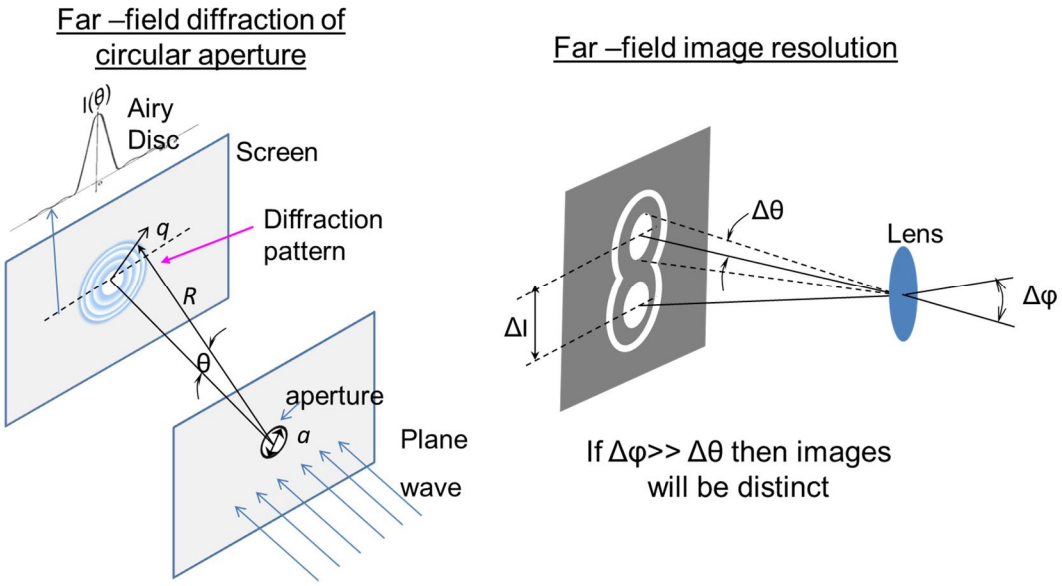

Figure 2.2: Analogy between diffraction through circular aperture and imaging resolution with a lens

The light diffraction also limits the resolving power of a traditional imaging system utilizing refractive optics such as lens. Based on Abbe's definition, the resolving power of an optical component is limited by the spreading out of each image point due to diffraction. Each image point in an object can be treated as a circular aperture and the resulting spread from each point forms an Airy disk on the imaging plane. When the two imaging points are close enough that the Airy disks from the two points overlap (Figure 2.2) then the two points become indistinguishable in the image and determine the resolution limit of the imaging system. Using the analogy with the circular aperture,

according to Abbe's criteria, the resolving power of a lens with focal length *f*, the lens diameter *D*, is given by:

$$q_1 = 1.22\frac{f\lambda}{D} = 1.22 * 2\pi * \frac{f}{k_o D} \tag{1.3}$$

where $k_o = 2\pi/\lambda$ is the maximum value of corresponding wave number. With the highest numerical aperture lens (i.e. $f/D \approx 0.5$) the resolution limit reaches roughly ~λ/2 (>200 nm for visible light).

The focusing ability of the lens is also determined by the diffraction limit with the same value as the imaging resolution based on the reciprocity relation [30]. Therefore, if traditional refractive and reflective optics (lens, mirrors) is used, the maximum resolution of laser based detection, imaging and fabrication is limited to >~λ/2 when the propagating light in far field is applied.

2.2 Far-field and Near-field

The resolution limit (i.e., ~λ/2) described in the previous section is only applicable in far-field where only the propagating light is utilized. Higher resolution, however, can be achieved in near-field. To understand the higher resolution in the near-field, the light wave propagation is represented with the Helmholtz equation (i.e. time-harmonic form of wave equation),

$$\nabla^2 E + k_o{}^2 . E = 0 \tag{1.4}$$

In this case, the electromagnetic wave *E(R,t)* can be represented with Fourier expansion of the electric field:

$$E(R,t) = \sum_{\sigma,k_r} E_\sigma(k_r).e^{(ik_z.z+ik_r.r-i\omega t)} \quad (1.5)$$

where k_z, and k_r are spatial components of wave vector $k_o = \sqrt{k_r^2 + k_z^2} = 2\pi/\lambda$.

In the far field range with propagating light, wave vectors in all directions should be real; therefore the wave vector k_r in the normal to propagation direction, which determines the spatial resolution on the imaging plane as must be less than $k_o = 2\pi/\lambda$., which lead to the far field diffraction limited resolution as in eq. 1.3 when $kr \sim k0$. In the near field range, however, k_r can be larger than k_o when k_z is imaginary, which corresponds to $E_z = E_o.e^{-\sqrt{k_z^2 - k_o^2 \varepsilon}.z}$ as an exponentially decaying field in z-direction. This exponential decay field in the transport direction is called *'evanescent wave'* and decays within a very short range (<<λ). As a result, the spatial resolution with evanescent wave ($k_r > k_o$) can be much higher than the far field diffraction limit.

2.3 Configurations of NSOM

The optical components which utilize the evanescent waves are named nano-optic devices. The idea of nano-optic devices is not new. However, due to the lack of modern fabrication and characterization methods, nano-optic devices were only at the conceptual level before ~1980's [12]. With the progress in micro/nano fabrication processes, micro/nanoscale characterization and detection methods in past few decades,

nano-optic devices have been fabricated and demonstrated for their capability in achieving nanoscale manipulation of light. The most common and perhaps the only commercially available nano-optic device is near-field scanning optical microscope (NSOM) [13].

The most common NSOM system developed in 1990's consists of an NSOM probe with an aperture much smaller than the wavelength of visible light (i.e. $<\lambda/2$). The aperture is brought in close proximity of a target either to illuminate or collect light from the target in near-field. The aperture is constructed on the sharp end of a conical optical waveguide such as optical fiber. The tapered region of the optical fiber is coated with a metal film to prevent leakage of light guided in the optical fiber. The sharp tip facilitates its positioning closer to the target irrespective of the roughness of the target. The NSOM can be configured in different modes depending on the illumination and collection of the visible light as shown in Figure 2.3.

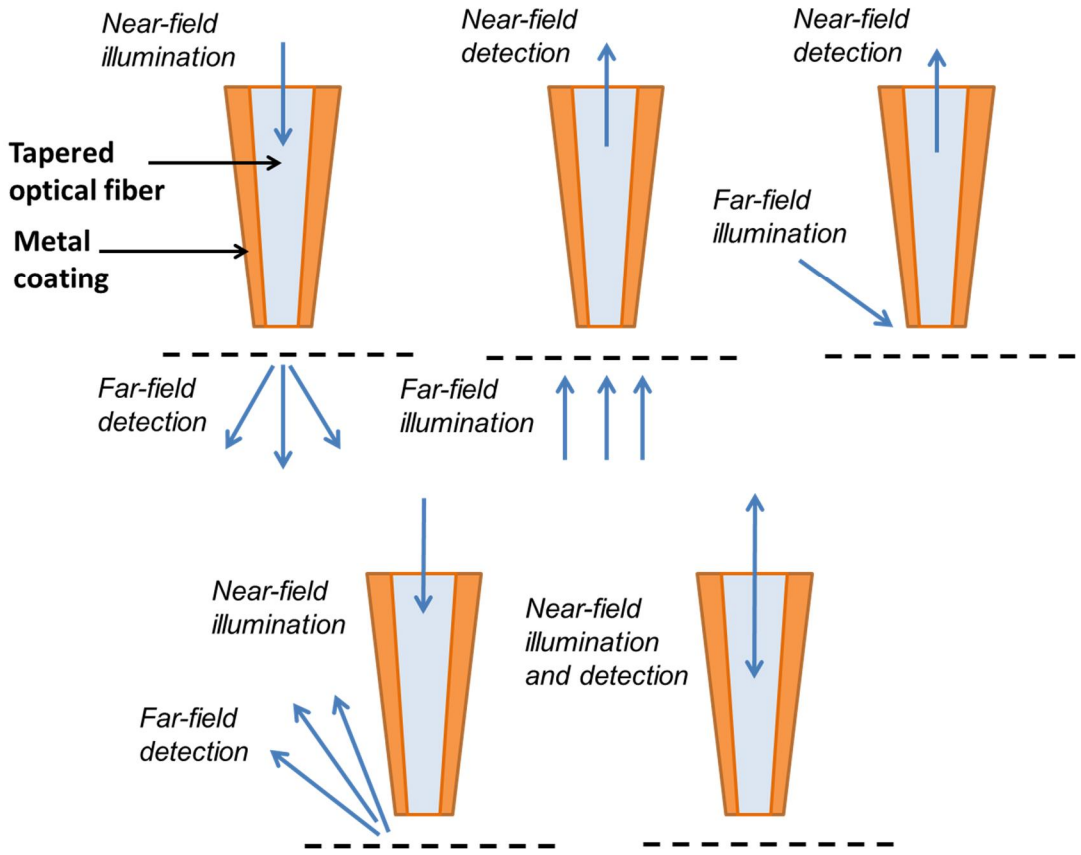

Figure 2.3: Modes of operation of NSOM: a) illumination mode, b) collection mode, c) reflection collection mode, d) reflection illumination mode and e) reflection illumination and collection mode

The resolution of optical imaging and contrast is determined by the aperture size and optimum distance control between target as the evanescent waves in near-field decays rapidly within a distance $<<\lambda$. The common method of nano-scale distance control is adopted from the scanning probe microscopy (SPM). The NSOM probe is mounted on a tuning fork which vibrates the NSOM probe with fixed frequency and amplitude. A piezo-electric module drives the probe closer to the target. As the probe

reaches closer to the target (<<λ) damping force due to Van der Waals interaction between probe and target is measured by the feedback system. The close loop control system maintains the driving motion of piezo-electric driver by measuring a set value to damping force. The NSOM is mounted on the tuning fork horizontally or vertically in either a shear-force or normal force (tapping mode) configuration respectively (Figure 2.4). A cantilevered configuration (figure 2.4c) is usually adopted in tapping mode. Other less common distance control mechanism in NSOM system is based on bouncing laser beam from the probe. The reflected beam from the probe is recorded with a photo-diode to maintain the position.

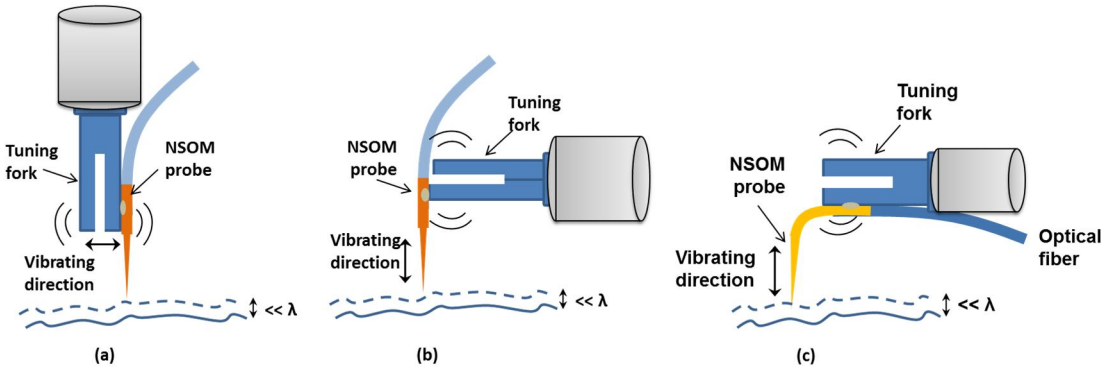

Figure 2.4: Configuration of distance control: a) Shear-force mode, b) tapping mode, c) tapping mode with cantilevered NSOM probe

2.4 Energy Transport and Heating of NSOM Probes

In most of the NSOM applications, high power laser is confined to a nanoscale region. Unfortunately, the light transport efficiency of NSOM probe is low ($<10^{-6}$-10^{-4}) and most of the light is absorbed by the metal coating of the probe [8]. The large light

dissipation in the metal coating and associated heating can result in thermal expansion and change in aperture size of the NSOM probe, which can lead to the change in throughput and deteriorate the recorded optical signal [14, 16, 17]. Also for NSOM imaging, a high temperature NSOM probe is not desired since a heated probe close to the sample (~10 nm) can heat and modify the sample significantly [18, 20, 26]. The NSOM probe can also be damaged if the light induced heating is too strong [21, 22, 27, 31, 32].

The light transport efficiency of NSOM probe is dependent on the structure and shape of the NSOM probe. To design an optimum NSOM probe for higher light transport and lesser heating effects in metal coating, it is important to analyze the light propagation through NSOM probe and estimate associated Joule heating of the metal coating. The problem can be divided into two parts, first the light propagation through the tapered optical fiber and second the thermal analysis of metal cladding.

Due to the complexity in the geometry of NSOM probe and characteristic size (i.e. aperture size $<\lambda/2$) wave type light propagation by solving Maxwell's equations is required. Previous studies have predicted the field propagation in a NSOM probe with various numerical methods, such as the Green function method [33, 34] the multiple multipole method [35], the finite-element method [36] and finite-difference time domain (FDTD) methods and body of revolution (BOR) FDTD methods [37, 38].

To incorporate the size effects, polarization and geometry effects, the wave propagation through NSOM probe to the target requires solving the time-domain

Maxwell's equations providing relationship between $\vec{E}$ (electric field), $\vec{D}$ (electric displacement), and $\vec{H}$ (magnetic field) using FDTD method:

$$\varepsilon_o \frac{\partial \vec{D}}{\partial t} = \nabla \times \vec{H} \tag{1.6}$$

$$\mu_o \frac{\partial \vec{H}}{\partial t} = -\nabla \times \vec{E} \tag{1.7}$$

Note that the standard 3D FDTD method requires an intensive computational effort and is time-consuming. This approach can be applied in time-domain analysis such as ultrafast target heating of target with NSOM probe and a femtosecond laser [38].

However, to analyze the nanosecond or longer laser pulse durations the wave propagation can be obtained from the time-harmonic Maxwell's equation providing relationship between $\vec{E}$ (electric field), $\vec{D}$ (electric displacement), $\vec{B}$ (magnetic induction) and $\vec{H}$ (magnetic field) within the NSOM probe is given by:

$$\nabla . \vec{D} = 0 \tag{1.8}$$

$$\nabla . \vec{E} = 0 \tag{1.9}$$

$$\nabla \times \vec{E} = -j\omega\mu\vec{H} \tag{1.10}$$

$$\nabla \times \vec{H} = j\omega\varepsilon_r\varepsilon_o\vec{E} \tag{1.11}$$

where ε_r is the relative permittivity of the material, ε_o=8.85418 × 10−12(F m−1) is the permittivity of free space and $\mu \approx 4\pi \times 10{-}7$(N A−2) is the permeability. The induced current density in the frequency domain is $J = j\omega D$. With this approach the time average joule heating Q_{av} at each location can be determined from $Q_{av} = (1/2).\mathrm{Re}(-j\omega E.D^*)$. The determined spatial distribution of joule heating from the optical analysis which is

valid for longer laser pulses (i.e. nanoseconds) provides the required initial distribution of the heat sources in the NSOM probe. The subsequent thermal analysis of the NSOM probe after the pulsed heating can be obtained from transient heat conduction

$$\rho_i c_i \frac{\partial T_i}{\partial t} = \nabla.(k_i \nabla T_i) + Q_{av} \tag{1.12}$$

where ρ_i is the density, c_i is the heat capacity and k_i is the conductivity of the materials (i.e. metal cladding and fused silica core of optical fiber).

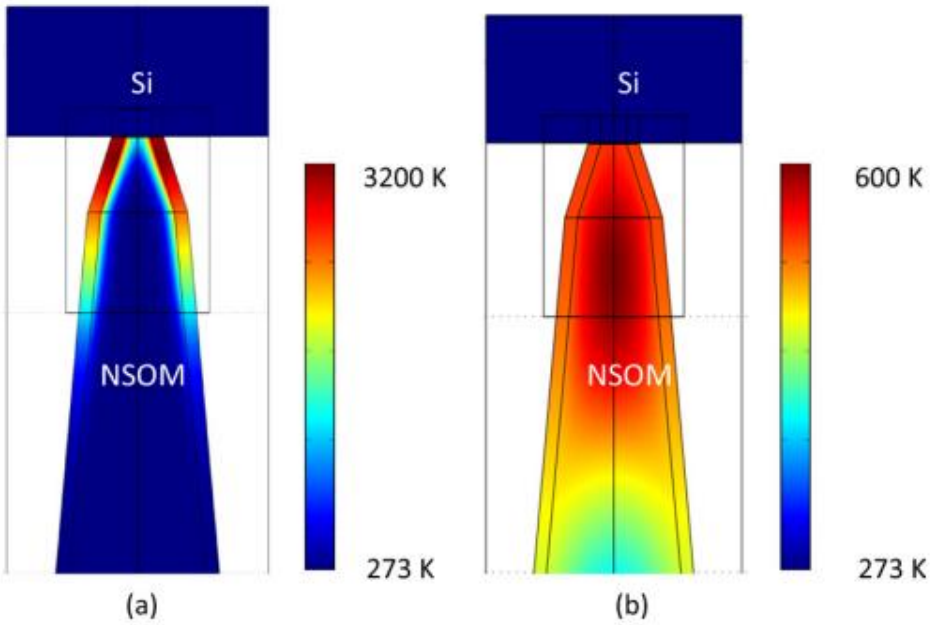

Figure 2.5 Temperature distributions a) during the 4 ns laser pulse and b) 100 ns after the laser pulse

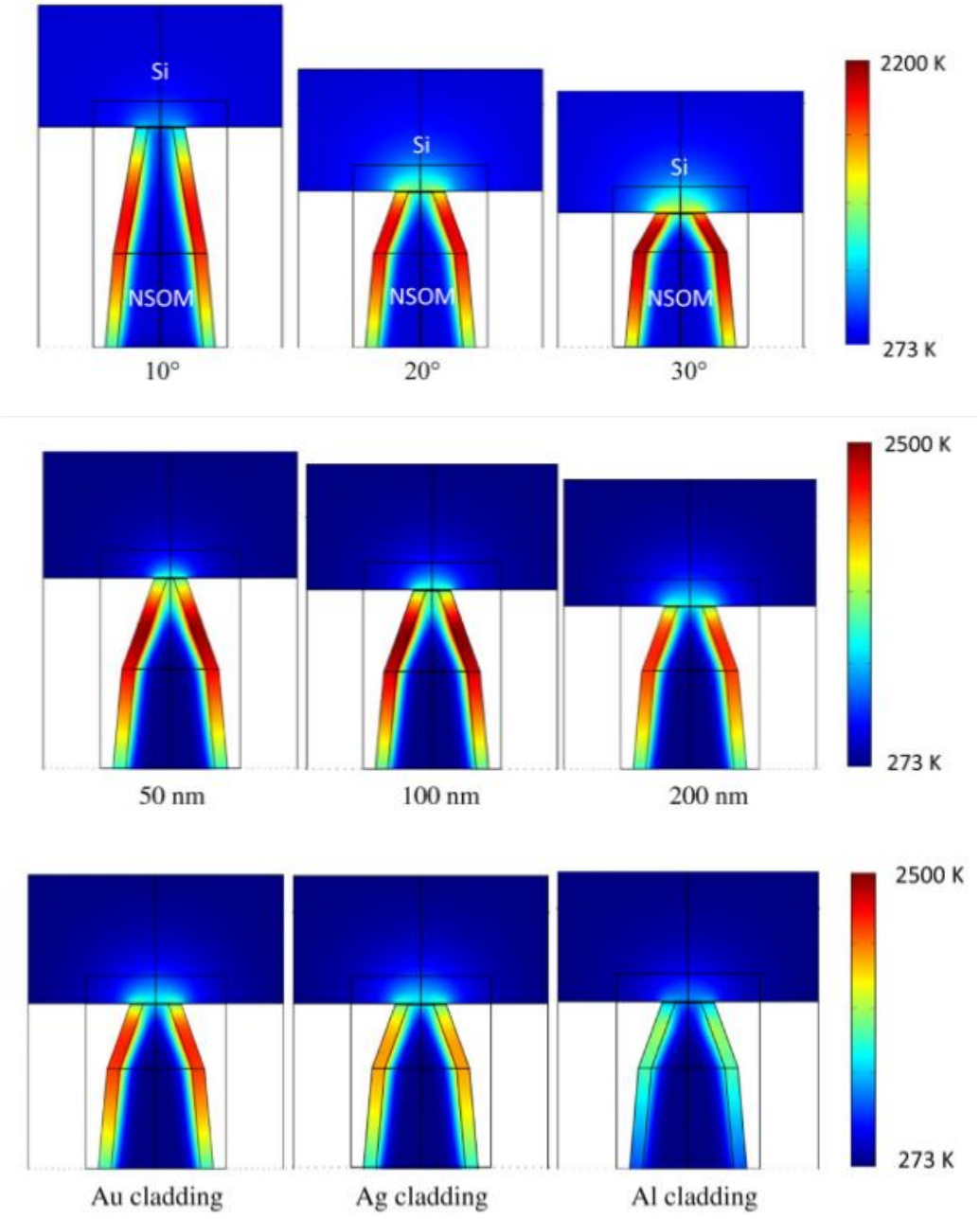

Figure 2.6: Effect of taper angle, aperture size and cladding material on temperature profile of NSOM probe

Based on this approach the temperature distribution of NSOM probe and a silicon target under nanosecond pulsed heating was obtained and effect of various parameters such as tapering angle optical fiber, cladding material and aperture size was studied [26]. Figure 2.5 shows the temperature distribution on the NSOM probe after the nanosecond laser pulse is delivered to NSOM probe and 100 ns after the laser pulse. Figure 2.6 also shows the effect of taper angle, aperture sizes, and cladding material on the heating effects of NSOM probe and target material.

From the theoretical analysis, it can be observed that the heating effects can be controlled by optimizing the size, shape and structure of the NSOM probe. However the theoretical analyses are based on several approximations which may not be valid in the real operation of NSOM probe. For example, the NSOM probe fabricated with fiber pulling method have continuous variation of tapering angle from tip to the bulk fiber (i.e., ~20° - ~3°), whereas all the simulation results reported in literature uses a single or double tapered geometry. The other geometric consideration such as uniform cladding thickness may also not be valid. In the thermal analysis the bulk properties (e.g., thermal and electrical conductivity) are considered. Though the metal cladding thickness is much larger than the electron and phonon mean free path, the thin film properties especially at the interface [39, 40] may be quite different. To validate the theoretical predictions of energy transport in NSOM probe (or other nano-optic devices), direct non-intrusive temperature measurement under different operating conditions is necessary. A methodology for non-intrusive temperature measurement and associated energy

transport analysis of NSOM probe under quasi-steady-state and transient conditions is developed in this research and described in chapter 6 and 7.

3. ANALYSIS OF NANOPATTERNING THROUGH NEAR FIELD EFFECTS WITH FEMTOSECOND AND NANOSECOND LASERS ON SEMICONDUCTING AND METALLIC TARGETS*

3.1 Introduction

As discussed in previous chapters, the confinement of laser light to deep sub-wavelength spot ($<\lambda/2$) can be achieved through a NSOM probe. Originally developed for high resolution optical microscopy, NSOM probes was quickly recognized as an important tool for surface modification [9]. It was proposed that if sufficient light intensity can be delivered from the NSOM probe to the target, the confined light from NSOM probe can be a potential tool for nano-machining. However, the small light transport efficiency and subsequent heating of NSOM probe can be a limitation in achieving nano-scale laser machining before it is thermally damaged.

Even with the limitations mentioned above, apertured NSOM probes were demonstrated for their ability in generating nano-patterns on polymer film with photo-sensitive dye [41]. The mechanism of nano-patterning was debated as nano-indentation due to thermal expansion of NSOM probes, ballistic mechanism, photo-chemical reaction and photo-thermal ablation [19, 41, 42]. In another group, nano-structuring of metal thin films was demonstrated with NSOM probe along with femtosecond laser pulses [43]. More recently, laser ablation on metal thin film with apertured NSOM probe

*Reprinted with permission from "Analysis of nanopatterning through near field effects with femtosecond and nanosecond lasers on semiconducting and metallic targets" by Sundaram V. M., Soni A., Wen S. B., 2010, J. Appl. Phys. **107**, 074305, Copyright 2010 by American Institute of Physics

with aperture sizes >λ, ~λ and <λ (but >λ/2) along with either femtosecond or nanosecond laser pulses was demonstrated [44] for potential application in high resolution chemical detection with LIBS (laser induced breakdown spectroscopy) [45-47]. With deep sub-wavelength apertured (i.e. <λ/2) NSOM probe and femtosecond laser pulses, nano-craters and nano-protrusions were generated on silicon wafer under different background gases [26, 48, 49]. The change of pattern shape from crater to protrusion was explained based on background gas effect.

From the above reported results, it was observed that the nano-pattern formation and the underlying mechanism of nano-patterning with sub-wavelength NSOM probe along with a pulsed laser is highly sensitive to the laser conditions, properties of target material and background gas. Since the previous experiments by different groups were conducted on different target materials under different experimental conditions (e.g, laser pulse duration, laser pulse durations, laser energy, and background gas), the exact mechanism of nano-patterning was not fully understood. Due to the lack of a proper understanding of nano-patterning mechanism it is difficult to achieve desired nano-patterning under certain experimental conditions. For example, it was demonstrated in some experimental and theoretical analyses that a combination of fs laser and NSOM probes with sub-diffraction limit aperture can generate nano-craters on pure silicon wafers. However, the same prediction may not be valid when fs laser is replaced with ns laser. Therefore, there is a need to conduct experiments with controlled conditions to study parameters which may affect the formation of nano-pattern on a target. By analyzing the results obtained from the controlled experiments, the mechanism of nano-

patterning, and the contribution of parameters such as material properties, laser conditions and background gas can be revealed.

To address the above issues and to better understand the characteristics and the mechanisms of nano-patterning with a combination of pulsed laser and NSOM systems along with their associated energy transport, my PhD study starts from experimentally characterize the nano-patterning with near-field effects and pulsed laser on different targets. Controlled experiments are conducted with various NSOM probes on different types of targets with pulsed laser under different laser conditions (e.g., laser energy, pulse duration and number of pulses). The contribution of each of these parameters on nano-patterning is discussed from the obtained results. The next section describes the experimental setup and experimental conditions used in this study.

3.2 Experimental Setup

Figure 3.1 illustrates the schematic of the experimental setup which is mainly composed of a commercial NSOM system (Nanonics Inc.) and a ns/fs pulsed laser source. For nanosecond experiment, Nd-YAG laser with optical parametric oscillator (OPOTEK Vibrant 355 II) operating at 409 nm and a pulse duration ~4 ns was utilized as the light source. For femtosecond laser experiments, Ti:Sapphire femtosecond laser (Spectra Physics) operating at ~401 nm with ~10 nm spectral width and ~150 fs pulse duration was utilized (Figure 3.1). The triggering of both lasers were synchronized with the commercial NSOM system (Nanonics Inc.) through a delay generator (SRS DG535). Emitted light from both lasers were conducted to the entrance of NSOM probes through an optical fiber coupler (Thorlab Inc.). A camsplice is installed in the middle of the

spliced NSOM optical fiber carrying laser energy from the optical fiber coupler to the NSOM tip. The laser energy carried with the optical fiber was measured at the spliced point with a pJ sensitive energy meter (Coherent Inc.). All the NSOM probes (purchased from Nanonics Inc.) have an aperture ~200 nm with a thin gold coating (~100 nm) outside in order to confine light to a sub-diffraction limit region around the NSOM tip. During the experiments, a constant separation (~10nm) distance between the NSOM tip and the targets was maintained through a closed loop control of the commercial NSOM system.

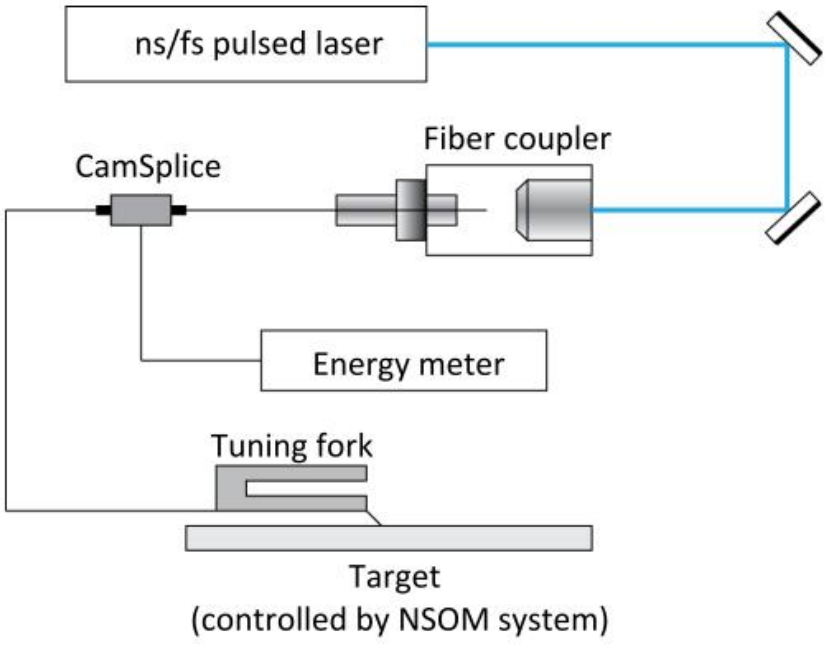

Figure 3.1: Schematic of experimental setup for nanosecond/femtosecond near field laser-material interaction

Targets examined in this study were pure silicon wafers, pure germanium wafers, and chromium /copper/silver thin film coatings (~250-300 nm) on quartz plates. The thin film metal samples were prepared with thermal evaporation (BOC Edwards 307 Evaporator). The depositions were conducted at ~10^{-6} Torr with a deposition rate of 0.02-0.2nm/s to ensure smooth surfaces. The generated nano-patterns after each experiments were scanned with atomic force microscope (Veeco, tip diameter <2nm) in order to obtain the topography images. To determine the presence of SiO_2 in the nano-patterns generated under different experimental conditions, Si samples after near field laser-material interactions were processed with buffered hydrogen fluoride solution (BHF 7:1) for ten minutes and then scanned again with the AFM. Note that BHF selectively etches silicon dioxide (SiO_2) and silicon nitride (Si_3N_4) with an etching rate of ~100 nm/min for SiO_2 and only ~0.5-1 nm/min for Si_3N_4 [12].

3.3 Results

The obtained experimental results with the above experimental setup in this research under different (a) target materials (Si, Ge, Cr and Ag), (b) pulse durations (fs vs. ns), (c) laser energy, and (d) number of laser pulses are grouped and listed as follows:

A. Near field laser-material interaction with semi-conducting materials (Si & Ge)

Silicon and germanium were selected as the experimental targets considering both materials have similar thermal properties but significantly different optical absorption coefficient at λ~400-410 nm (Table 1). Ge has much higher absorption coefficient than Si at λ~400-410 nm. Through comparing the experimental results from Si and Ge respectively, we expect to reveal the contribution of optical absorption

coefficient in the near field laser-material interaction along with the associated mechanisms in nano-pattern generation. The results from Si and Ge with ns and fs laser pulses are listed as follows:

Table 1: Optical and thermal properties of silicon and germanium

	Boiling Temperature (K)	**Heat of Evaporation (kJ/mol)**	**Reflectance (%)**	**Absorption coefficient (cm^{-1})**	**Conductivity ($W \cdot m^{-1} \cdot K^{-1}$) At 300K**	**Thermal diffusion length (cm) in 4 ns**
Silicon	3538	369	42.72	0.964×10^5	149	$6x10^{-6}$
Germanium	3106	334	45	6.66×10^5	60.2	$4x10^{-6}$

a. For nanosecond laser pulses

Si: Nano-patterns were observed on intrinsic Si wafers when E > ~1.8 – 2.0 nJ after 300 pulses. The shape of the nano-pattern remained a protrusion for different number of laser pulses (i.e. 300 to 1200 pulses, Figure 3.2 & Table 2). The diameter of the nano-protrusions generated in air varied from 1200 nm to 1400 nm while the height of the protrusions increased from 6 nm to 18 nm (Table 3) after 300-1200 laser pulses.

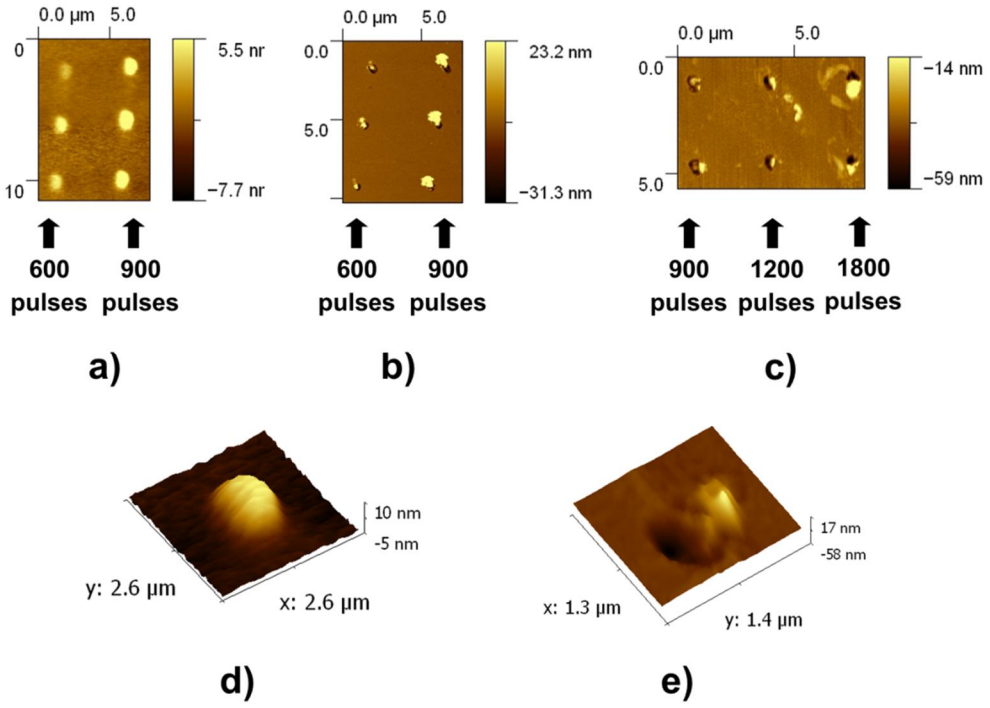

Figure 3.2: Patterns generated with nanosecond laser a) on silicon wafers before BHF etching, b) on silicon wafers after BHF etching, c) on germanium wafers; 3D nano-pattern shape after 900 pulses d) on silicon and e) on germanium

Ge: Nano-patterns were observed on intrinsic germanium wafers after 50 laser pulses when the input laser energy was >1.7 nJ, which is about 0.1-0.3 nJ lower than the damage threshold of Si wafers. Unlike the patterns generated on silicon, the nano-patterns generated on germanium were in crater format for all the number of laser pulses studied (figure 3.2). The diameter of the nano-patterns increased from 700 nm to 900 nm after 900-1800 laser pulses (Table 2) while the depths of the protrusions increased from 15 nm to 25 nm after 600-900 pulses (Table 3).

b. For femtosecond laser pulses

Si: Nano-patterns were observed on intrinsic Si wafers with femtosecond laser all the three laser energies studied (i.e., 1, 2 and 3 nJ). The shape of nano-patterns evolved from nano-craters (for single and few pulses) to nano-protrusions gradually when the number of laser pulses increased from 50 to 300 for all the three laser energies studies (c.f., figure 3.3). The diameter of the nano-patterns increased from 500 nm to 1000 nm (Table 2) while the depth of the protrusion increased from 8 nm to 50 nm at E ~2nJ (Table 3) after 50-600 laser pulses.

Ge: Nano-patterns were also observed on intrinsic germanium wafers with femtosecond laser, for all the three laser energies studied (i.e., 1, 2 and 3 nJ). Compared with the results on Si wafers, the resulting patterns on intrinsic germanium wafers were nano-craters for all laser energies and number of laser pulses studied (i.e., 1 to 600 pulses, figure 3.3). The diameter of the nano-craters varied from 500 nm to 900 nm (Table 2) while the depth of the nano-craters increased from 15 nm to 55 nm (Table 3) after 50-600 laser pulses.

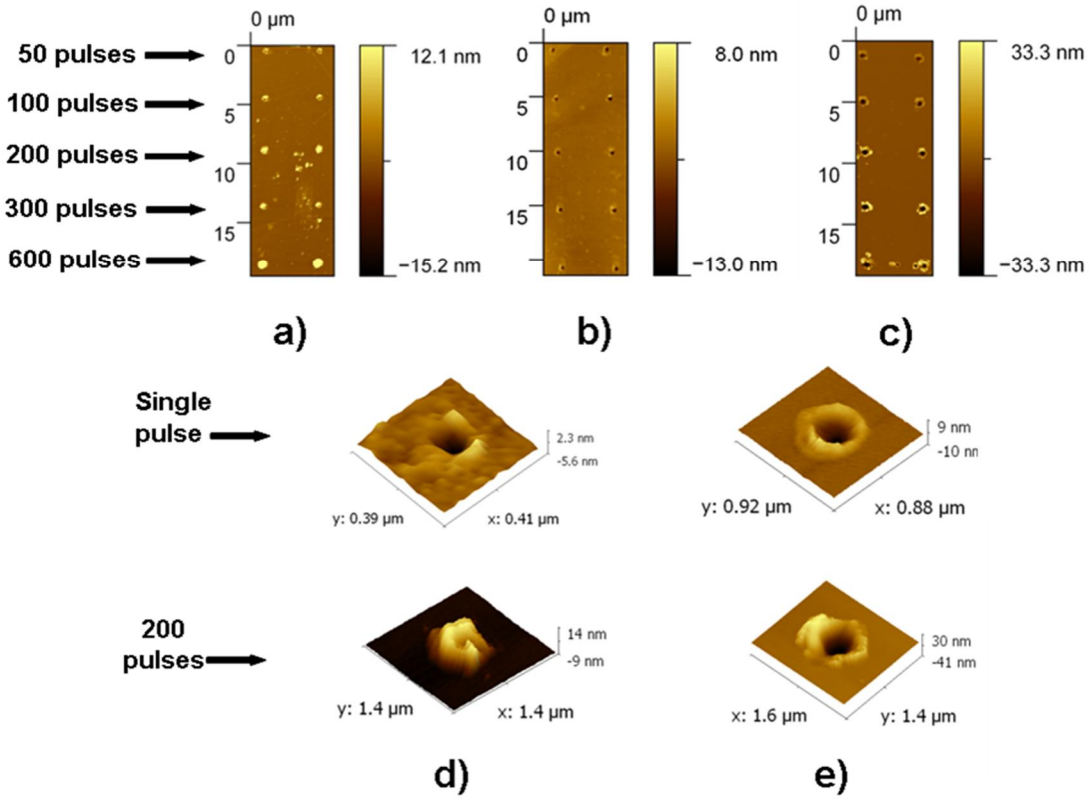

Figure 3.3: Nano-patterns generated with multiple number of femtosecond laser pulses (a) on silicon before etching with BHF, (b) on silicon after etching with BHF for 2 minutes, (c) on germanium; 3D nano-pattern shape e) on silicon after single (nano-crater) and 200 femtosecond laser pulse (nano-protrusion) and d) on germanium after single (nano-crater) and 200 femtosecond laser pulse (nano-crater)

Table 2: Nano-pattern size (i.e., average diameter of nano-crater/nano-protrusion) for silicon and germanium

Number of Laser pulses	Nanosecond Laser		Femtosecond Laser	
	Silicon (nm)	Germanium (nm)	Silicon (nm)	Germanium (nm)
50	Not observable		500±50	500±50
100	Not observable		600±50	600±50
300	1200 ±200		800±100	700±100
600	1300 ±200		1000±50	900±100
900	1400 ±200	700±200		
1200	1400 ±200	800±200		
1800		900±200		

B. Near field laser-material interaction with metallic thin film coatings (Cr and Ag)

Chromium and silver were selected in the near field laser-material interaction with metallic materials considering their similar physical properties but significantly different surface reflectivity at λ~400-410 nm. The surface reflectivity of silver is ~10 times higher than that of Cr (Table 4). We expect to reveal the contribution of surface reflectivity in the near field laser-material interactions through comparing the nano-patterns generated on these two metallic materials. The results from Cr and Ag with nanosecond and femtosecond laser pulses are listed as follows:

Table 3: Nano-pattern size (i.e., average height of nano-protrusions and depth of nano-craters) for silicon and germanium

Number of laser pulses	Nanosecond Laser		Femtosecond Laser	
	Silicon (nm)	Germanium (nm)	Silicon (nm)	Germanium (nm)
50	Not observable		8±3	-15±5
100	Not observable		10±5	-30±10
300	6 ±2		20±10	-50±10
600	10 ±2		50±10	-55±20
900	15 ±3	-15 ±2		
1200	18 ±3	-20 ±2		
1800		-25 ±2		

a. For nanosecond laser pulses

Cr: Nano-patterns were observed on the Cr film with ns laser after 100 laser pulses when E~1.8-2nJ. The shape of nano-patterns evolved from nano-craters to nano-protrusions gradually. This transition happened when the number of laser pulses >200 (figure 3.4). The diameter of nano-craters varied from 400nm to 600nm for 100-200 laser pulses (Table 5). Once the nano-protrusions were generated under larger number of laser pulses, the diameter of protrusions kept increasing with respect to number of laser pulses while the height increased slightly from 10nm to 20nm after 600 -1000 laser pulses (c. f. figure 3.4 & Table 6).

Ag: No observable patterns were generated on silver surfaces even after 2000 laser pulses when E ~1.8–2.0 nJ or even under the damage threshold energy of NSOM probes (i.e. E ~2.5-3.0 nJ).

Table 4: Optical and thermal properties of chromium, copper and silver

	Boiling Temperature (K)	**Heat of Evaporation (kJ/mol)**	**Reflectance (%)**	**Absorption coefficient (cm^{-1})**
Copper (film thickness 250nm)	2835	300.4	3.7	~6.86×10^{5}
Silver (film thickness 300nm)	2435	250.58	82.1	~6.14×10^{5}
Chromium (film thickness 300nm)	2944	339.5	4.3	~1.13×10^{6}

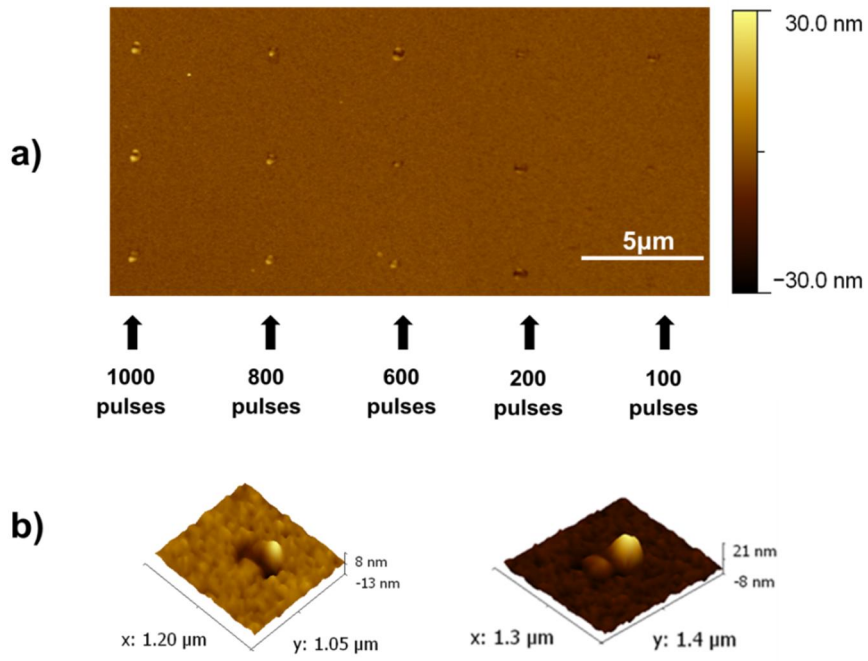

Figure 3.4: Nano-patterns generated on Cr with a) multiple nanosecond laser pulses and b) 3D nano-pattern shape on Cr with 50 laser pulses to 1000 laser pulses

b. For femtosecond laser pulses

Cr: Nano-pattern were observed on Cr targets with femtosecond laser pulses under all the laser energy studied (i.e., 1, 2 and 3 nJ). The patterns changed from nano-craters under single laser pulse to nano-protrusions for multiple laser pulses studied in air (i.e., 50, 100, 200, and 300 pulses) (c.f. figure 3.5). The nano-craters with single laser pulse have a diameter ~600 nm (figure 3.5) when E~2 nJ. The diameter and the nano-patterns show little dependence on the number of laser pulses studied even when protrusions were formed (Table 5). However, the height of nano-protrusions increased from 15 nm to 50 nm when the number of laser pulses increased from 50 to 300 laser pulses (Table 6).

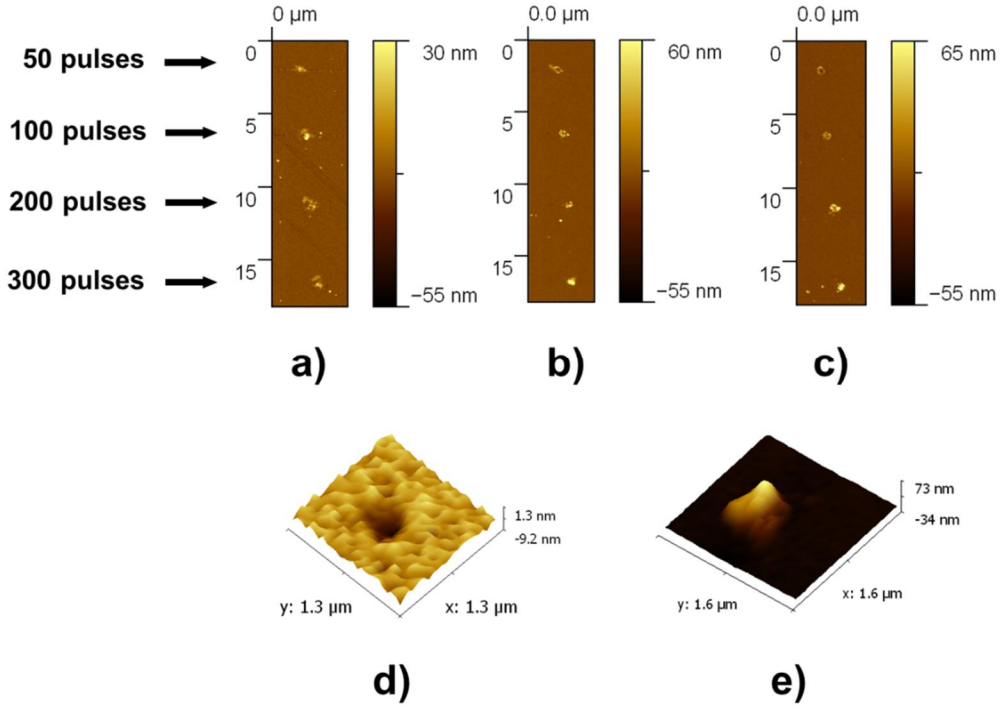

Figure 3.5: Nano-patterns generated on Chromium in air with multiple femtosecond laser pulses when a) E~1 nJ, b) E~2.0 nJ and c) E~3.0 nJ; 3D nano-pattern shape on Cr with femtosecond laser with E~2.0 nJ d) after a single pulse and e) after 300 pulses

Ag: No observable patterns were generated on silver surfaces even after 2000 laser pulses with all three input laser energies studied (i.e., ~1, 2, and 3 nJ). Note that 3 nJ is the maximum fs laser energy available to be coupled to the NSOM probe under the present experimental setup.

Table 5: Nano-pattern sizes (i.e., average diameter) for chromium, copper and silver

Number of laser pulses	Nanosecond Laser		Femtosecond Laser	
	Chromium (nm)	Silver (nm)	Chromium (nm)	Silver (nm)
50		Not observable	600±100	Not observable
100	400±100	Not observable	700±100	Not observable
200	500±100	Not observable	800±100	Not observable
300	500±100	Not observable	900±100	Not observable
600	600±100	Not observable		Not observable
800	600±100	Not observable		Not observable
1000	600±100	Not observable		Not observable

Table 6: Nano-crater depths for chromium and silver

Number of laser pulses	Nanosecond Laser		Femtosecond Laser	
	Chromium (nm)	Silver (nm)	Chromium (nm)	Silver (nm)
50	Not observable	Not observable	40±5	Not observable
100	-4±2	Not observable	50±5	Not observable
200	-6±2	Not observable	50±8	Not observable
300		Not observable	55±8	Not observable
600	10±2	Not observable		Not observable
800	15±4	Not observable		Not observable
1000	20±4	Not observable		Not observable

3.4 Discussions

In the above paragraphs, we listed the evolutions of size and shape of nano-patterns in different targets under different experimental conditions. To obtain a general picture for the mechanisms responsible for nano-patterning which is the focus of this study, we examine the influence of optical parameters on nano-pattern generation from the experimental data. From these connections, we are able to link the generation of nano-patterns to the potential physical mechanisms which can qualitatively explain the obtained results under the conditions studied. In the following paragraph, we first discuss the influences of (a) laser pulse duration, (b) laser pulse energy, and (c) number of laser pulses (i.e, optical parameters) on the pattern generation with combination of NSOM systems and pulsed laser sources. The proposed physical mechanisms, which are responsible for nano-pattern generation in this study, are presented after the following discussion.

A. Contribution of laser pulse duration

For all the materials studied in this research, femtosecond laser generated patterns on targets with lower threshold energy compared with the nanosecond laser under the same number of laser pulses. In addition, patterns generated with fs laser are sharper with cleaner edges (figure 3.3). In contrary to the lower damage threshold to the targets, the damage threshold of NSOM probes is significantly increased with fs laser (> 3 nJ) compared that with ns laser (<2.5-3 nJ).

Besides the contribution to the damage threshold of the NSOM probes and the targets the laser pulse duration also affect the chemical composition of the resulting nano-

patterns on different targets. We selected Si as an example in this study. Though protrusions were generated on Si targets for large number of fs and ns laser pulses in air, the protrusion generated from fs laser can be entirely removed with BHF while the protrusions generated from ns laser cannot be entirely removed with BHF. The BHF etching results suggest that the protrusions generated on Si wafer in air with ns laser has components in addition to SiO_2. Through the additional examination of the protrusions generated with ns laser (i.e. through EDS, XRD and TEM scanning), we found that these protrusions are composed with a significant amount of nano-crystalline Si which did not appear in fs results [50]. A detailed discussion of this study is given in chapter 4.

B. Contribution of number of laser pulses

For all the materials studied in this research (i.e., Ge, Si, and Cr), the size of the nano-patterns, more or less, increased with respect to the number of laser pulses. However, the pattern shapes may change with respect to number of laser pulses (note that this statement is not true for silver on which we observed no patterns). The change in the shape of the nano-patterns happened in Si with fs laser pulses and Cr with both ns and fs laser pulses. For the above three experimental conditions, the shape of patterns evolved from nano-craters to nano-protrusion when the number of laser pulses increased. We noticed that the major difference between Si/Cr group (on which the resulting nano-pattern shape showed dependence on the number of laser pulses) and Ge target (on which the resulting nano-pattern shape showed no dependence on the number of laser pulses) is their oxidation compounds. Stable oxidation compounds (i.e., SiO_2 for Si and Cr_2O_3 for Cr) are formed on Si and Cr surfaces under low temperature heating (i.e.,

<~500 K). However, close to melting temperatures are required for forming GeO_2 on Ge surfaces.

C. Contribution of laser energy

For ns experiments, fixed pulsed laser energy (i.e., E ~1.8 – 2.0 nJ) was utilized because no patterns were observed when E<1.6 – 1.8 nJ along with the fact that the NSOM probes were damaged when E> 2.5 – 3.0 nJ. Experiments with femtosecond laser were conducted under three different energies namely E~1, 2 and 3 nJ. Note that the NSOM probes remain healthy under all three energy levels studied with fs laser. An increase in the pattern height/depth was observed when the input fs laser energy was increased (figure 3.6). The pattern shapes and diameters, on the other hand, showed little dependence on the fs laser energy for the experimental conditions studied.

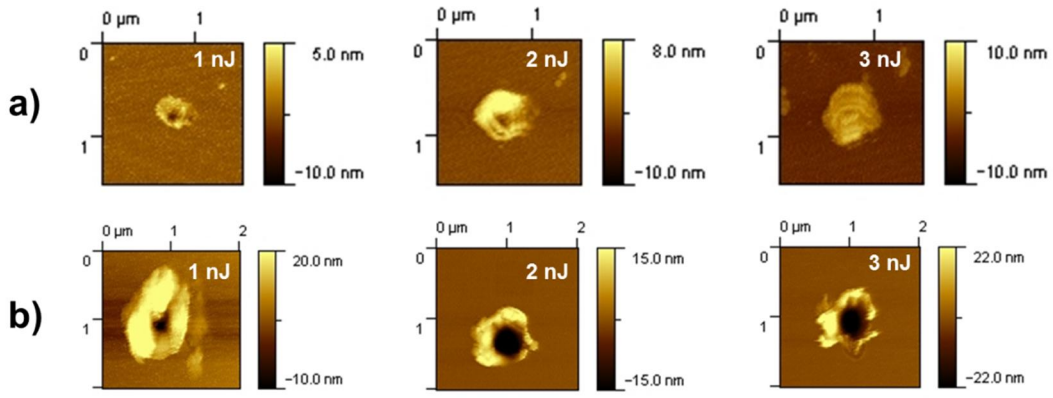

Figure 3.6: Patterns generated after 100 laser pulses using femtosecond laser for E = 1, 2 and 3 nJ on (a) Silicon wafer (b) Germanium wafer

Based on the observed contribution of optical parameters listed above, a physical picture which is an extension from traditional microscale laser-material interaction is

established to explain the optical/thermal energy transport from the NSOM probe to the targets along with the resulting nano-pattern generation. These physical pictures fits with the experimental data obtained in this study and allow us to predict the results for future experiments under similar experimental conditions. A description of this physical picture is as follows:

When ns laser was applied, significant light dissipation (mainly around the NSOM tip) is converted into the thermal energy of the NSOM probe considering >99.9% of optical energy is dissipated into heat during the transport within the NSOM probe [51], the NSOM probe maintains a very high temperature around the tip while carrying intense ns laser pulses [52]. As a result, in addition to the optical energy transport from the NSOM probe to the target through near field effects, there is a considerable amount of thermal energy transport from the NSOM probe to the target during the experiments when ns laser pulses are applied. This additional thermal energy transport induced by ns laser pulses can melt the sample (which was observed on Si targets) or even the metal cladding of the NSOM probes (c.f., figure 3.7) as we observed in this study when light intensity is above the threshold.

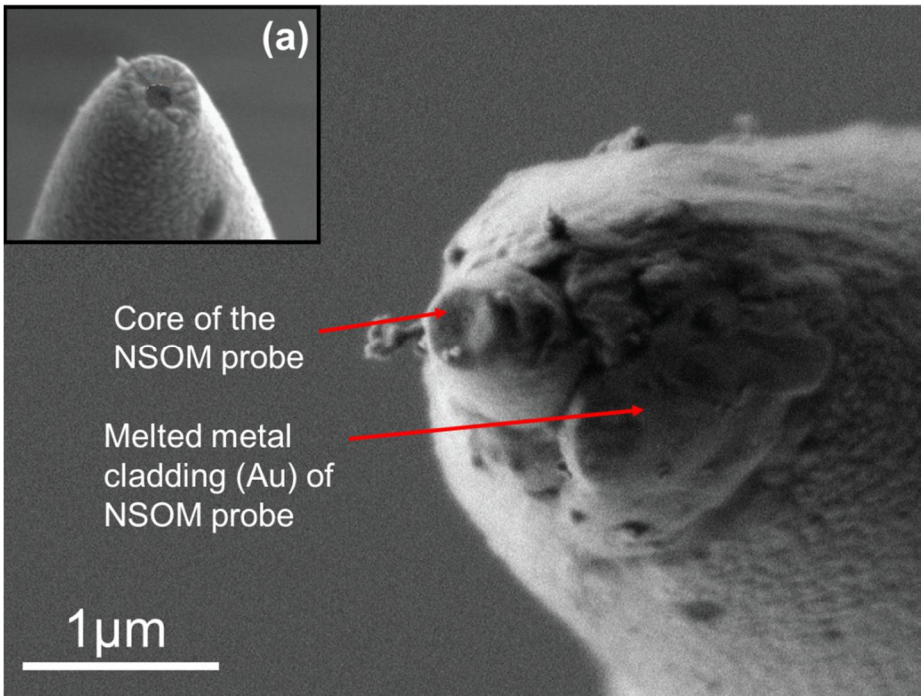

Figure 3.7: SEM images of a probe with laser induced thermal damage indicating the gold melt region obtained from EDS analysis and (a) a new NSOM probe

When fs laser was applied, the light fluence at the target with fs laser is ~10^4 times higher than that with ns laser under the same E values. Due to the extremely high laser fluence associated with fs laser pulses, non-linear (e. g., multiphonon) light absorption especially for semiconducting materials is important. Strong surface heating or even coulomb explosion [7] on semi-conducting materials can be induced through non-linear optical absorption compared with ns laser cases. As a result, patterns are formed on targets will lower threshold energy compared with that under ns laser pulses. In addition to the non-linear optical absorption, the ultrashort pulse duration with fs laser reduces the characteristic time for thermal diffusion (or heat affected zone, HAZ) in the

targets. The smaller thermal diffusion region provides a better confinement of thermal energy, which causes higher temperature in a small region around the laser spot when fs laser is applied. Consequently, the pattern generation threshold is further reduced with femtosecond laser if we consider the thermal effects induced by fs laser pulses. The physical picture for fs laser-material interactions explains the reduction of the damage threshold of Cr, Si and Ge targets in this study (which are the three targets on which nano-patterns were observed) when fs was applied compared with ns laser results.

Besides lowering the damage threshold of the target, due to the ultrahigh photon fluence associated with fs laser pulses, photoelectron emission can be induced at the metal cladding of NSOM probes due to the high photon fluence when fs laser pulses are carried through the NSOM probes [53]. The emission of electron carries a significant amount of absorbed EM energy in the metal cladding to the surrounding. As a result, the NSOM probes can maintain a low temperature when they are operating with fs laser pulses. Consequently, much high energy fs laser pulses can be transported with NSOM probes without any thermal damages compared with ns laser cases. This statement is supported with the SEM observation of the NSOM probes after operating with fs and ns laser pulses.

Three main mechanisms [54] can be induced on the targets after absorbing energy from NSOM probes and are responsible for the nano-pattern generation in this study. These three mechanisms are (a) nanoscale laser ablation of the target, (b) nanoscale oxidation resulting from nanoscale heating of the target, and (c) nansocale recrystallization resulting from nanoscale melting of the target. Nano-craters on the

target can be formed through nanoscale laser ablation while nano-protrusion can be formed either through nanoscale oxidation or nanoscale recyrstallization of the targets. Note that more than one mechanism may attribute to the nano-pattern formation in each experimental condition. The pattern formation induced by multiple mechanisms is especially important when more than one laser pulses is applied.

When more than one laser pulses were applied to the targets, change in size and shape of the nano-patterns as function of number of laser pulses can be understood from following three scenarios,

i. Nano-crater is first generated for single or few laser pulses due to nanoscale laser ablation. The crater depths keeps increasing with respect to the number of laser pulsed since the additional laser ablations keep removing material from the target. Nano pattern formation following this scenario was observed on targets on which oxidation layers are difficult to be formed at low temperatures (e.g., Ge with ns and fs lasers).

ii. Nano-crater is first generated with single pulses due to nanoscale laser ablation. Surrounding the ablated crater is an oxidation layer on the heated target. The thickness of the oxidation layer increases with respect to the number of laser pulses. As a result, the separation between the NSOM probe and the intrinsic target becomes longer and longer when the number of laser pulses is increased. The semiconducting oxides (or metallic oxides) act as a buffer layers between NSOM tip and the intrinsic target. Consequently, near field light intensity at the intrinsic target surface from the following laser pulses becomes weaker because

of the thicker oxidation layer, which increases the separation between the NSOM tip and the intrinsic target. After certain number of laser pulses, the effective light intensity at the intrinsic target is not enough to induce a nano-scale laser ablation. After that only oxidation resulting from laser heating of the target can occur and dominates the patterns formation, which causes the transition of pattern shape from nano-craters to nano-protrusions. Nano-pattern formations following this trend were observed on targets on which oxidation layers are formed under low temperatures (e.g., Si with fs; Cr with ns and fs).

iii. Nano-protrusion is first generated for single or few laser pulse since the energy is not enough to ablate the target. The protrusions can be formed either from nanoscale oxidation [55] or nanoscale melting and recrystallization of the target [50]. The height of protrusion increases slowly with respect to the number of laser pulses due to the increased separation distance between the NSOM probe and the intrinsic target when the protrusions were formed. Nano-pattern formation following this trend was observed on targets with high ablation threshold and low oxidation temperature (e. g., Si with ns).

When the laser energy is increased, as long as it is higher than the pattern generation threshold, the efficiency of ablation and/or oxidation is enhanced. Deeper craters or higher protrusions were generated on the same target through ablation and oxidation separately when the fs laser energy is increased. Note again that we didn't vary the ns laser energy in this study since the damage threshold of the target is very close to the damage threshold energy for NSOM probe.

The above physical picture describes the energy transport from NSOM probe to the target along with the target response and associating nano-pattern generation as functions of optical conditions and the chemical properties of the target material. The physical picture does fit with the experimental data obtained in this research under all the conditions studied.

A sharper picture can be obtained when we compare the results on different targets under the same optical conditions. From this comparison the contribution of optical properties of different materials on nano-pattern formation can be revealed. The first example is the significant differences in pattern size and shapes on Si and Ge. Both materials have similar optical reflectivity under the wavelength tested. In addition, both materials have similar thermal properties (i.e., thermal conductivity and heat of vaporization (Table 1). However, because of the smaller band gap of Ge (~6 eV) compared with Si (~11 eV), Ge has absorption coefficient ~7 times higher than that of Si (Table 1). A surface type light absorption occurs in Ge compared with a more volumetric type light absorption in Si. The stronger light absorption in a smaller volume induces a strong mass removal during near field laser material interaction on Ge compared with that on Si under the same laser conditions (c.f., figure 3.8). As a result, larger craters were observed on germanium surfaces under all the experimental conditions studied (note that there are even no craters observed on Si surfaces under certain experimental conditions). Another example obtained in this study is the dramatic difference in the pattern formation on Cr and silver. No pattern was observed on Ag surfaces under all the experimental conditions studied. The zero pattern generation on silver in this study can

be attributed to its extremely high surface reflectivity (~90%) compared with Cr (<~5%) at λ~400-410 nm. Little amount of incident light from the NSOM tip enters the silver target due to this extremely high surface reflectivity, which prevents nano-pattern generation (c.f., figure 3.9).

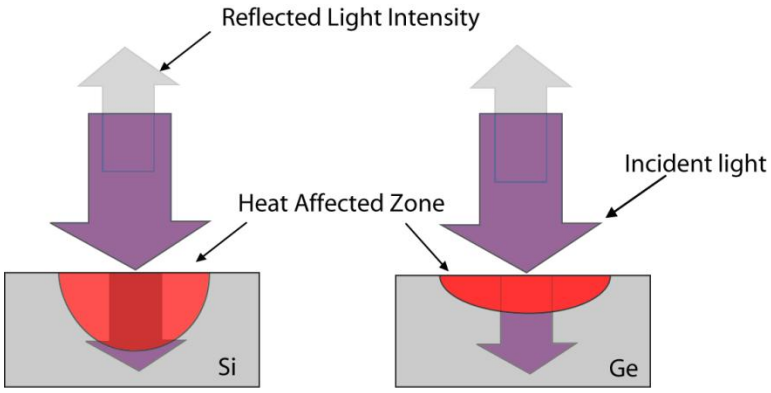

Figure 3.8: Schematic of the effect of sample absorption coefficient on nano-pattern generation

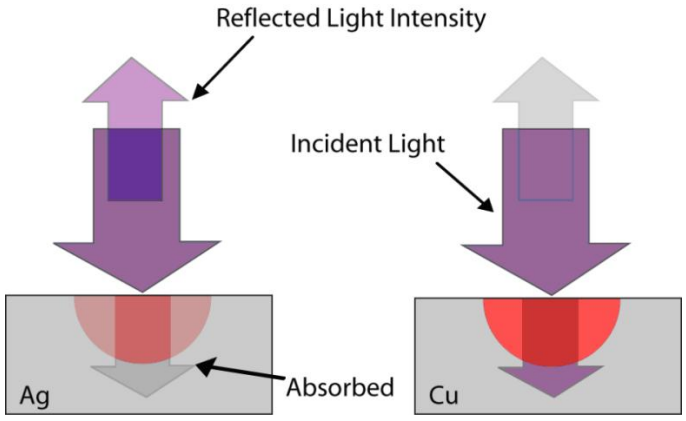

Figure 3.9: Schematic of the contribution of surface reflectivity on nano-pattern generation

A supplementary ns laser experiment has been conducted on Cu in air in order to verify the physical picture we obtained in this study for understanding the nano-patterning on targets as a function of optical/chemical properties of the targets. Cu has similar thermal properties compared with silver and Cr. Like Cr, Cu has very low surface reflectivity ($\tau \sim 0.08$) at λ~400-410 nm. However, compared with Cr, copper oxide can only be formed efficiently under high temperature [56]. Therefore, because of the absence of thick oxidation layers, we expected to get nano-craters on Cu under all the experimental conditions studied. The supplementary experimental results do fit with our prediction. When ns laser was applied to the Cu target with NSOM, nano-craters with diameter ranged from 300 to 600 and depth ranged from 5 nm to 7 nm were observed after 900 to 1800 number of laser pulses when E ~ 2 nJ (figure 3.10 & Table 7).

Table 7: Nano-craters diameter and depth for copper

Number of Laser Pulses	**Nano-crater diameter (nm)**	**Nano-crater depth (nm)**
900	300±100	-4±2
1200	500±100	-5±2
1800	600±100	-7±2

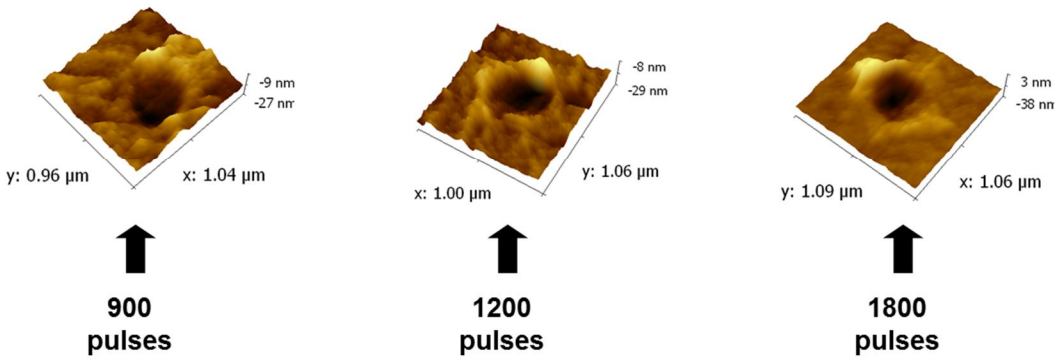

Figure 3.10: Patterns generated on copper after 900, 1200 and 1800 using the nanosecond laser

3.5 Summary

Near field nano-patterning through NSOM probes was conducted on selected semi-conducting targets (i.e. Si and Ge) and metallic targets (i.e. Cr, Cu and silver) at λ ~400-410 nm. The contributions of laser pulse duration (i. e., fs vs. ns), number of laser pulses, and laser energy on different targets were studied with controlled experiments in this research. Based on the results, fs laser showed a prevention of the NSOM probes from damages under high laser energy while thermal damages of NSOM probe was observed with ns laser pulses when E>2.0-2.5 nJ. Furthermore, because of the non-linear optical absorption along with a smaller HAZ, the damage threshold of targets with fs laser pulses (<1nJ) is much lower than that with ns laser pulses (~1.8-2.0 nJ) when they are delivered with NSOM probes to the targets.

The formation of the nano-patterns on different targets can be explained with nanoscale laser ablation, nanoscale oxidation and nanoscale melting/recrystallization on

the targets. The increment of input laser energy merely enhanced the pattern formation mechanisms and the resulting size of the patterns on the targets under all the experimental condition studied. The number of laser pulses, however, can change the size and the shape of the resulting patterns on different targets. For materials on which both nanoscale ablation and nanoscale oxidation dominate nano-pattern generation (e.g., Si & Cr), the contribution of nano scale ablation become weaker in the following laser pulses due to a thick oxidation layer from previous laser pulses. The thick oxidation layer reduces the light intensity at the intrinsic target and prevents further nanoscale laser ablation on the targets after certain number of laser pulses.

Besides the contributions of the optical (laser) conditions on nano-pattern formation, the optical properties of the targets can significantly change the resulting nano-patterns obtained from a combination of NSOM probes and pulsed lasers. Targets with higher absorption coefficient formed larger craters due to a stronger energy absorption within a confined area on the targets. Targets with higher surface reflectivity, on the other hand, experience limited laser-material interaction during each laser pulse, which results in small or even no craters after the experiments.

When ns laser is applied in the study, a hot NSOM provides additional energy transport (i.e. thermal energy transport) compared with that with femtosecond laser. This additional thermal energy transport can lead to thermally induced modification of the target surface (e.g., melting and nanoscale recrystallization of the heated spot on the target (e.g. silicon)). To detailed understand the additional thermally induced surface modification with NSOM probes when ns laser is applied and may not exist with fs

laser, we performed a microscopic target characterization of the target around the spot where intense laser energy is transported from the NSOM probe. The detailed description in presented in the next chapter.

4. NANO-PATTERN GENERATION ON PURE SILICON WAFER IN ARGON AND AIR WITH SUB-DIFFRACTION NANOSECOND LASER PULSES*

4.1 Introduction

The femtosecond results presented in the last chapter under different energy, material and background gas conditions can be appropriately explained with nanoscale oxidation and ablation. The dominant mechanisms for the formation of nano-patterns with fs laser were oxidation when oxygen was presents in the background gas. When oxygen was absent, e.g. with pure argon as the background gas, laser ablation was dominant and nano-craters resulted after multiple laser pulses. However, such explanation cannot be applied for the corresponding results with ns laser. For example nano-protrusions formed in the air as a background gas with the nanosecond laser pulses on silicon target could not be removed through the BHF etching suggesting that the nano-protrusion may not be due to oxidation of silicon. Also, nano-craters were not observed on silicon in the nanosecond experiments even with the highest possible laser pulse energy (i.e. ~2.5 nJ)

It is expected that mechanism in addition to mass removal through ablation should happen with ns laser and are attributed to these abnormal results. Note that no nano-patterning results have been published with a combination of nanosecond laser and

*Reprinted with permission from "The generation of nano-patterns on a pure silicon wafer in air and argon with sub-diffraction limit nanosecond laser pulses" by Soni A., Sundaram V. M., Wen S. B., 2010, J. Phys. D: Appl. Phys. (43) 145301, Copyright 2010 by IOP Publishing

sub-diffraction limit apertured (<0.5 λ) NSOM probes. There is a concern whether this combination can provide enough energy transport to a target compared with a previous femtosecond study since the ablation threshold with a nanosecond laser is considerably higher than that with a femtosecond laser particularly for semiconducting materials. To identify these additional mechanisms, and to answer these questions, we conducted another detailed experimental study for generation of nano-patterns on silicon wafers with multiple nanosecond laser pulses through near field light transport in different background gas (e.g., air and argon). The chemical composition of nano-patterns formed after large numbers of laser pulses were examined with chemical analysis tool (i.e. EDS) as we expected that these protrusions could be composed of other chemicals than silicon oxides. Also, the physical structure of nano-protrusions was analyzed with TEM to identify any possible recrystallization of silicon oxide after melting and cooling. The details of the experimental conditions and subsequent chemical and physical analysis are discussed in next sections.

4.2 Experimental Conditions

In this study, the same experimental setup illustrated in previous chapter (Figure 3.1) is used. NSOM probes with ~ 200 nm aperture diameter and ~ 100 nm gold cladding (UV NSOM probe purchased from Nanonics Inc.) were utilized. Nanosecond laser pulses from an OPO system (OPOTek Vibrant 355 II) at a wavelength of 409 nm and a pulse width of ~ 4 ns were selected as the light source. The selected wavelength is larger than two times the diameter of the aperture, which satisfies the sub-diffraction limit requirement of this study. Pure intrinsic silicon wafers were used as the targets for

comparison with our previous femtosecond experiments. Both air and argon were selected as the background gases. The surface topography images were determined first from an NSOM scanning and then from a high resolution scanning with an atomic force microscope (Veeco AFM) before and after each experiment. The consistent results from the double scanning scheme ensure the reliability of the obtained surface topography after each experiment. To analyze the chemical composition of the nano-patterns, the samples after the experiments were (a) dipped in a buffered hydrogen fluoride solution (BHF 7:1) for 2 min and then scanned again with an AFM, (b) examined with an energy dispersive x-ray spectrometer (EDS) and an x-ray photoelectron spectroscope (XPS), (c) diced with a focused ion beam (FIB) and then studied with a transmission electron microscope (TEM).

4.3 Results and Discussions

The characteristics of the nano-patterns generated in air and in argon separately through a combination of a NSOM probe and nanosecond laser pulses are listed as follows. Note that the pattern shape shows no dependence on the number of laser pulses and the pattern size increases linearly with respect to the number of laser pulses. Also, the pattern heights are too shallow to be determined with AFM when the pulse number is less than 50. Therefore, only results from a large number of laser pulses are presented.

i. When air was used as the background gas, nano-protrusions were generated on silicon wafer surfaces after multiple nanosecond laser pulses for an input laser energy of ~ 1.8–2 nJ. The diameters of protrusions increased from 1000 to 1200 nm and heights increased from 6 to 15 nm when the number of laser pulses

increased from 600 to 900 (Figure 4.1(a)). Note that the protrusions formed on the silicon surface in air cannot be dissolved by the BHF solution, which are different from those obtained with a femtosecond laser (Figure 4.2). Therefore, these nano-protrusions generated in air are not composed of SiO_2 only.

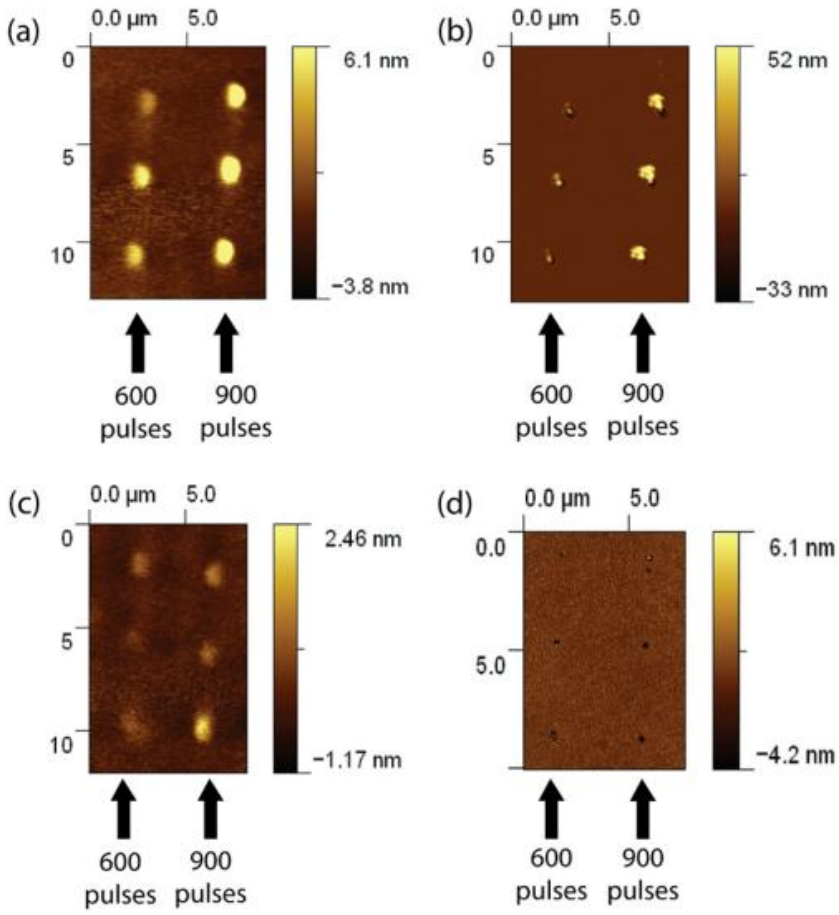

Figure 4.1: Nano-patterns generated on pure Si wafer with nanosecond laser pulses: (a) in air before BHF processing, (b) in air after BHF processing, (c) in argon before BHF processing and (d) in argon after BHF processing

ii. When argon was used as the background gas, similar nano-protrusions were generated on the silicon surface after multiple nanosecond laser pulses for an input laser energy of 1.8–2 nJ. These protrusion results with a nanosecond laser in argon are entirely different from the crater results obtained with a femtosecond laser in argon in a previous study [48]. The diameter of the protrusions increased from 1000 to 1100 and the heights changed slightly from 2 to 4 nm when the number of laser pulses increased from 600 to 900 (Figure 4.1(c)). However, unlike the protrusions formed in air, these much smaller protrusions can be completely etched into nano-craters after immersing them in the BHF solution (Figure 4.1(d)). The diameter of these craters obtained after etch is ~ 250 nm with depths of ~ 4–6 nm.

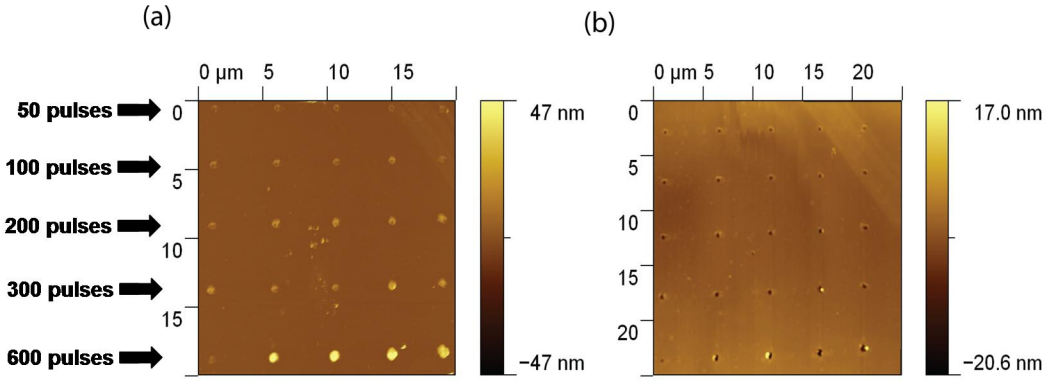

Figure 4.2: Nano-protrusions after 50, 100, 200, 300 and 600 femtosecond laser pulses (E ~ 2 nJ) (a) before BHF processing and (b) after BHF processing

Since no nano-craters were observed on the targets even in Ar after thousands of laser pulses, we concluded that laser ablation is not one of the major pattern generation mechanisms when nanosecond laser pulses were applied on Si targets. Note that the selected nanosecond laser energy (E ~ 1.8–2 nJ) is very close to the maximum laser energy which can be afforded with the selected sub-diffraction limit NSOM probe. Slight damage (i.e. melting of the metal cladding of the NSOM probes) was observed when E > ~ 2.5–3.0 nJ after <100 laser pulses. Therefore, it is adequate to claim that laser ablation cannot be achieved on Si targets through a combination of a nanosecond laser and sub-diffraction limit NSOM probes on Si targets before the damage of the probes. Note that no damage of the NSOM probe was observed after all the number of laser pulses tested when the energy was less than the damage threshold.

To determine the formation mechanism of nano-protrusion with nanosecond laser pulses, we examined the chemical compositions of the protrusions first. Three chemical elements exist around the sub-diffraction limit confined laser spot during the experiments, namely gold (the metal cladding of the NSOM probe), SiO_2 (the core of the NSOM probe and the intrinsic oxidation layer of the silicon wafer) and Si (the target material). EDS and XPS were applied to check the chemical composition of the nano-protrusions. Both EDS and XPS spectra showed no evidence of gold element on the target. Therefore, the protrusions formed on the silicon surface in air, which cannot be fully dissolved with BHF, should be due to the presence of a significant amount of pure silicon. The protrusions formed on the silicon surface in Ar, which can be fully dissolved with BHF, should be composed mainly of SiO_2.

To further understand the generation mechanisms of nano-protrusions under nanosecond laser pulses, we generated a large protrusion (~ 120 nm in height and ~ 1 μm in width) in air after ~ 3000 laser pulses when E ~ 2.8 nJ. The nano-protrusions were diced with a FIB and then examined with TEM (Figure 4.3). According to the TEM images, the nano-protrusions are actually a hump of a large recrystallized region composed of SiO_2 and nano-crystalline silicon (nc-Si). This recrystallized region is separated from the Si base by a flat and uniform SiO_2 layer. Although the SiO_2 layer is pretty flat in most regions, the TEM image showed a very slight extension of the SiO_2 layer into the Si base in the region beneath the centers of the nano-protrusions. The diameter of this additional extended SiO_2 region into the Si base is ~ 100–200 nm with depths < ~ 10 nm into the Si base.

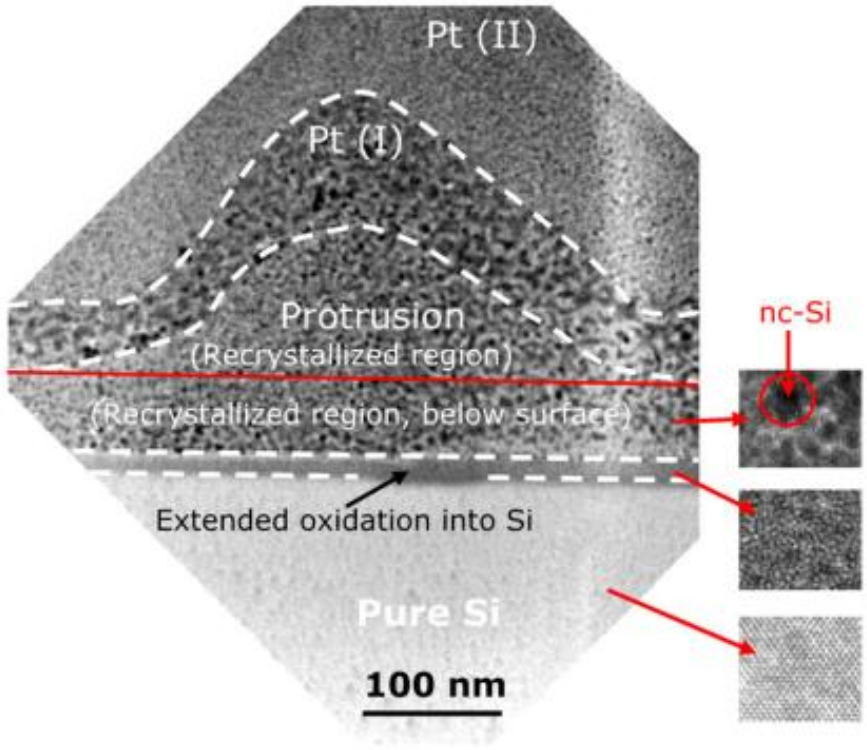

Figure 4.3: TEM image of a cross section of nano-protrusion generated on a silicon wafer with nanosecond laser pulses. Pt(I) and Pt(II) are the two platinum layers deposited on the sample before the FIB dicing. The solid red line corresponds to the average surface level before Pt deposition. The dashed white lines are superposed on the TEM image to provide an approximated interface among regions

The formation of the nc-Si cannot be due to a pure oxidation process. However, through fast melting and recrystallization of the existing SiO_2 region, abundant nc-Si can be formed in the recrystallized SiO_2. A similar example is the microscale direct laser heating (annealing) of silicon rich (or pure) SiO_2 with nanosecond (or longer duration)

laser pulses, which results in microscale protrusions (>10–20 μm) composed of nc-Si and SiO_2 [21, 57]. We suggest that a similar mechanism can be attributed to the formation of nano-protrusions composed of SiO_2 and nc-Si in this study. The formation of a large protrusion on Si in air with nanosecond laser pulses can be understood from a sequence of physical processes as follows:

i. The intrinsic SiO_2 layer is melted and recrystallized into a small protrusion (composed of SiO_2 and nc-Si) resulting from the optical/thermal energy transport from the NSOM probe to the target during and after the first nanosecond laser pulse.

ii. An additional thin SiO_2 layer is formed beneath the recrystallized region due to the oxygen diffusion into the Si base shortly after the nanosecond laser pulse.

iii. The recrystallized region along with the underlying SiO_2 layer from the previous laser pulses are melted and recrystallized by the following laser pulses. As a result, the size of the nano-protrusion is increased after each laser pulse in air. More and more nc-Si will be present in the nano-protrusion after each laser pulse, which prevents the nano-protrusion from getting entirely etched with BHF.

For the experiment in Ar, since there is no continuous oxidation of the Si base as described in step II due to the lack of oxygen atoms, the increase in the protrusion height is very limited compared with the results in air. Also, the size of the protrusion in Ar does not increase obviously with respect to the number of laser pulses. Much fewer nc-Si are present in these smaller protrusions in Ar, which allows the protrusions to be entirely removed with BHF. When the SiO_2 is removed with BHF, nano-craters of diameters ~

100–200 nm and depths of ~ 4–6 nm are revealed at the end of BFH etching for experiments in Ar. These shallow craters correspond to the shallow extension of the SiO_2 layer into the Si base as indicated in the TEM image (Figure 4.3). The formation of this additional shallow SiO_2 , since it overlaps with the regions where strong light intensity appears during the experiment, can be attributed to the laser enhanced oxygen diffusion from the recrystallized region to the Si along with the resulting formation of shallow SiO_2 in the Si base.

The lack of melting and recrystallization mechanisms in nano-pattern formation in previous femtosecond experiments but important in the present nanosecond laser study can be understood from the significant heating of NSOM probes with intense nanosecond laser pulses but not with femtosecond laser pulses. The significant melting of the NSOM probe after conveying intense nanosecond pulses (i.e. ~ 2.5–3 nJ), which was not observed in femtosecond experiments, is strong evidence of the heating of the NSOM probe with nanosecond pulses but not with femtosecond laser pulses.

Although a lower nanosecond laser energy (E ~ 1.8–2 nJ) was applied in this study to prevent the damage of the NSOM probes, the temperature of the probe can still approach the melting (~ 1337 K) or even boiling temperature (~ 3129 K) during the experiment [26]. The hot NSOM probe can transport its thermal energy directly to the target surface through conduction and radiation. The strong thermal energy transport from the NSOM probe to the target can result in the melting and recrystallization of the target and the formation of nano-protrusions. Such strong thermal energy transport does not appear in experiments with femtosecond laser pulses, which prevents the formation

of the melting and recrystallization structure in our previous study. Note that the heat transfer phenomena associated with the hot NSOM probe (e.g. the thermal expansion of the NSOM probe due to the high temperature) induced by nanosecond laser pulses are difficult to observe with the existing NSOM systems. The existing NSOM systems have a feedback control frequency of < ~ 100–300 kHz, which is not enough to capture the transient heating phenomena induced by a nanosecond laser pulse with a characteristic time scale of ~ tens to hundreds of nanoseconds.

4.4 Summary

In summary, when a nanosecond laser was combined with a sub-diffraction limit NSOM system for nanoscale laser patterning, laser ablation is no longer one of the dominant pattern generation mechanisms on Si targets. Instead, the nano-protrusions are formed primarily due to the melting and recrystallization of the Si target along with the possible oxidation of Si base when O_2 is present in the background gas. These unique nano-protrusions are composed of SiO_2 and a significant amount of nc-Si which was not observed in previous femtosecond experiments. The melting and the recrystallization of the target, which are important with nanosecond laser pulses but not observed in previous femtosecond experiments, can be attributed to the strong heating of the NSOM probes when they are operating with nanosecond laser pulses. The hot NSOM probes transport a significant amount of thermal energy to the target, which results in the melting and formation of nc-Si rich recrystallized structures on the Si targets. Through proper control of the melting and recrystallization mechanisms with nanosecond laser pulses along with the oxidation and ablation mechanisms observed in previous

femtosecond experiments, we expect that a versatile nanoscale direct patterning methodology can be achieved with a sub-diffraction limit NSOM system by controlling the optical conditions during the experiments.

From this study, one of the major concerns when using nanosecond laser is significant heating effects of NSOM probe. This limits the ability to achieve laser ablation through NSOM probe with nanosecond laser pulses. In most academic and industrial applications, a nanosecond laser is the more preferred pulsed light source compared with a femtosecond laser considering its lower cost and ease of maintenance. There is a concern whether this combination can provide enough energy transport to a target since the ablation threshold with a nanosecond laser is considerably higher than that with a femtosecond laser particularly for semiconducting materials. On the other hand the damage threshold of NSOM probe with nanosecond laser is still too low (e.g., ~2.5-3.0 nJ in this study).

5. NON-INTRUSIVE TEMPERATURE MEASUREMENT OF NSOM PROBES WITH THERMOREFLECTANCE*

5.1 Introduction

Light induced heating in the metal cladding of NSOM probe leads to malfunctioning (noise in the signal, thermal stress and thermal expansion) and ultimate failure under higher laser intensities. The low light transport efficiency and the resulting undesired heating effects are the major concerns in adopting NSOM probe for sub-wavelength laser processing/machining. To conquer these limitations, correlations between the NSOM configuration and the associated heating under different operating conditions should be identified through a detail study of energy transport and resulting temperature evolution in NSOM probe [35, 58]. The corresponding theoretical analysis is presented in chapter 2 and provides us a basic understanding. However, due to the limitation of computation resources, the theoretical model is very simplified and need to be justified with a direct measurement of temperature distribution in the NSOM probe during operation [26, 38].

Indirect assessment of the temperature profile of NSOM probes has been carried out in 90's through measuring the thermal expansion of the probe and relate the expansion to the temperature field with a combined optics-energy transport analysis [14-16, 22, 59, 60]. Direct temperature measurement was carried out with single point

*Reprinted with permission from "Non-intrusive temperature measurement of NSOM probes with thermoreflectance imaging" by Soni A., Wen S. B., 2012, J. Phys. D: Appl. Phys. (45) 185101, Copyright 2012 by IOP Publishing

thermoreflectance measurement [28] and with micro thermocouple [27]. In the micro-thermocouple measurements, a temperature profile was obtained by measuring temperature at different locations along the tapered region of the NSOM probe. Temperature measurement with micro thermocouple provides the spatial resolution limited to few microns (i.e., size of the thermocouple probe). Also, the thermal capacitance of the thermocouple can significantly affect the accuracy of the temperature measurement especially when the size of NSOM probe is less than a few microns. A single point thermoreflectance, on the other hand, provides a nonintrusive measurement, which is preferred. However it is a time consuming approach to measure the temperature profile of the entire NSOM probe and relies on high reproducibility of the experimental results under the same conditions.

A direct non-contact 2D temperature imaging through recording the change of the optical reflectance as a function of the surface temperature can be utilized in determine the temperature profile of the NSOM probe in a time-efficient manner [61-65]. A charge coupled device (CCD) camera based thermoreflectance measurement was adopted in this study to obtain a 2D thermal image of NSOM probe in place of integrated photo detectors in traditional single point thermoreflectance [66]. Review of this newer thermoreflectance method can be found in the references [61]. The spatial resolution of the deployed 2D thermoreflectance can be close to diffraction limit (e.g. <300 nm) with a temperature resolution ~10mK [67, 68]. Through this time-efficient nonintrusive method, we studied dependences of the energy transport in the NSOM probes under different operation conditions. Contributions of the key parameters on the

temperature profile of NSOM probes determined with the 2D thermoreflectance method are presented in the following sections.

5.2 Thermoreflectance Imaging (Homodyne Method)

Thermoreflectance imaging is a non-contact optical method which measures change in temperature from the change in the reflectance of the object under periodic heating [61]. The change in the reflectance of a metal surface is almost linearly proportional to the change in the surface temperature and can be related with the following:

$$\Delta T = \left(\frac{1}{R} \frac{\partial R}{\partial T} \right)^{-1} \frac{\Delta R}{R} = (\kappa)^{-1} \frac{\Delta R}{R} \tag{1.13}$$

where 'κ' is the thermoreflectance coefficient, and is of the order 10^{-4}/K for most metals. An appropriate choice of probing wavelength for the given sample can ensure a higher 'κ' and hence the sensitivity of the thermoreflectance imaging [69]. In the homodyne thermoreflectance imaging, the required high single to noise ratio (i.e., $O(10^{-4})$) for thermoreflectance imaging is achieved through averaging 1000's of images to diminish the random noises recorded during the measurements [68].

5.3 Experimental Setup

Figure 5.1 illustrates the experimental setup for the homodyne thermoreflectance imaging of the NSOM probe. A highly stable DPSS laser (100mW, 532nm, DPSS Laser System, OEM Laser Systems Inc.) was used as a probe laser. The NSOM probe was heated with diode lasers of different wavelengths (405 nm or 650 nm). A non-polarizing beam splitter (NBS) was used to direct the probe laser beam to illuminate the NSOM

probe with an objective lens (OBJ). Due to the coherence property of probing laser, speckle patterns from random optical interference are generated in the images of the NSOM probes. There are several ways to remove speckles in imaging such as by spinning the azimuthal incidence angle [70], using a oscillating reflector [71] or using fast scanning micro-mirror [72]. In this set-up, a diffuser (ground glass diffuser 1500 GRIT, Thorlabs) mounted on a high frequency vibrating stage was installed before the beam splitter to provide diffused illumination in order to avoid speckles in the optical imaging. The probe beam was enlarged to provide an even intensity distribution over the object plane. Vibrating diffuser provides additional divergence and evenness to the probe beam. The NSOM probe was mounted on a tilt platform assembled to an x-y translation stage so that position and tilt angle could be adjusted. The reflected images were captured with a 16-bit depth B/W CCD camera (Opteon 1000 base T camera 120 fr/s, Opteon Corporation) externally triggered with a pulse generator (Model 575 pulse/delay generator, Berkeley Nucleonics Corporation) to achieve the required capturing frequency. The pulse generator was also synchronized with a function generator (Model 645 50MHz function/arbitrary waveform generator, Berkeley Nucleonics Corporation) to control the emission of the laser diode. The heating of NSOM probe follows almost the square waveform of the pump laser from laser diode with a small phase lag due to thermal diffusion. The main phase lags which can cause the measurement error are the thermal diffusion through the depth of the metal coating

(~100 nm) and the thermal diffusion of the metal coating along the NSOM probe (~350 μm). The diffusion time for the two length scales are ~0.07 ns and ~0.96 ms respectively [73]. Both time scales are much smaller than the smallest modulation time (~31 ms) used in this study. Therefore, the error in the thermoreflectance imaging due to phase lag in thermal cycle may not be significant in the selected experimental conditions of this study. The input power of the pump laser to the NSOM probe was measured with a power meter (Coherent Inc., Model LaserMate Q) at the fiber end before each experiment as illustrated in Figure 5.1. The spatial resolution of the set-up is determined either by the diffraction limit or the digital resolution of the camera (the larger one among the two values). The spatial resolution of our imaging is ~1.1 μm limited by the digital resolution based on the effective NA 0.29, 10X magnification and CCD pixel size 5.5 μm. The temperature resolution is estimated based on the number of images captured (>5000) and bit depth of CCD camera (16 bit). The detailed relation can be found in [68]. Based on the relation, the resolution of our temperature measurement is <1 K.

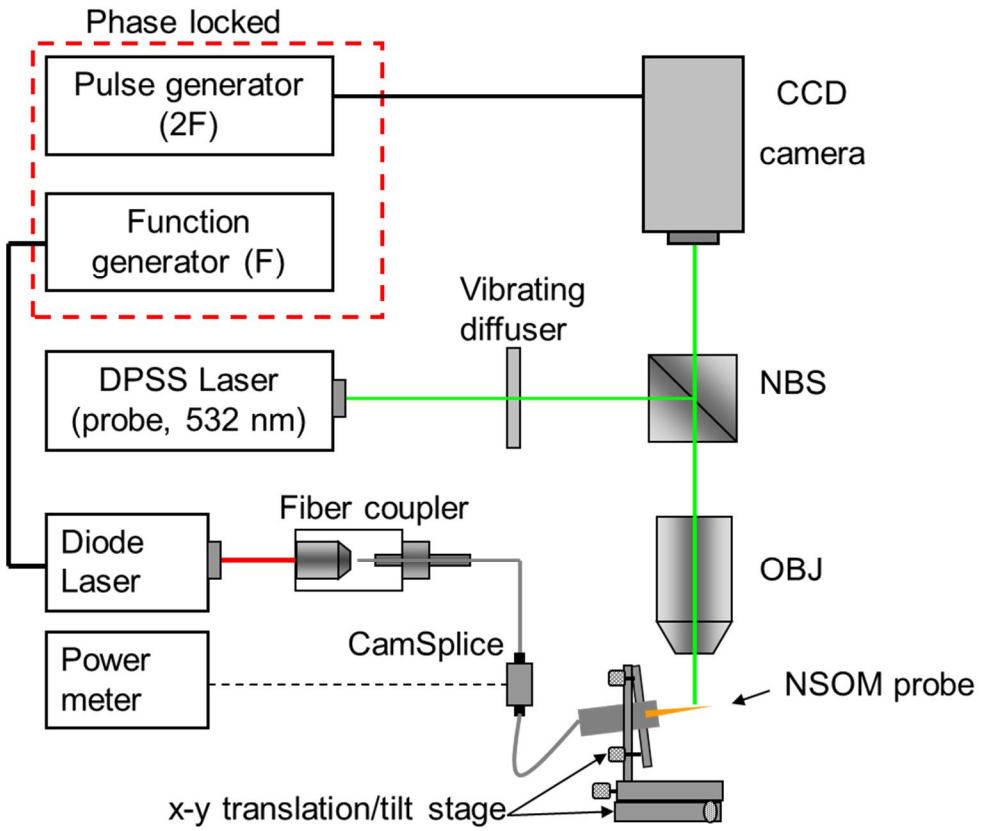

Figure 5.1: Schematic of the experimental setup for homodyne thermoreflectance imaging of NSOM probes

Two different type of NSOM probes were selected at the beginning of the study, namely, (a) gold coated cantilevered NSOM probes (Figure 5.2) and (b) gold coated straight NSOM probes (both from Nanonics Imaging ltd.). A large deflection of the cantilevered NSOM probe (>1 μm) due to laser induced heating was observed even with low laser intensity (<1mW). Since any observable deflection can destroy the required precision of thermoreflectance imaging, straight NSOM probe (showing no deflection under all laser energy tested) rather than cantilevered NSOM probes were used for the

thermoreflectance experiments. Note that the straight NSOM probes may also show deflection during periodic heating if the metal coating and/or the shape of pulled fiber is non-symmetric. The straight NSOM probes from Nanonics Imaging Ltd. used in the experiments showed no observable deflection for all experimental conditions used in this study.

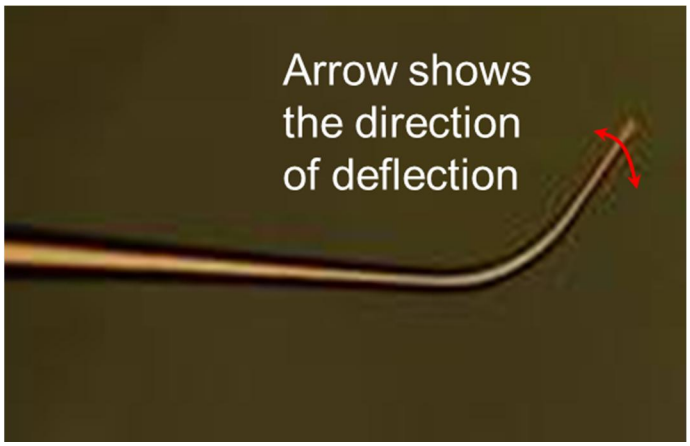

Figure 5.2: Optical image of cantilevered NSOM probe (courtesy: Nanonics Imaging Ltd.), the direction of deflection of probe during cyclic heating is shown

The SEM images of the straight NSOM probe used in the experiments are shown in Figure 5.3. It is observed that the tapering angle of the NSOM probe changes continuously from the pulled tip to the bulk region. The tapering angle varies slowly from 7° (5-100 µm) to 3° (100-500 µm). When it is very close to the tip (i.e. <5 µm) the taper angle increases sharply to 10°-20°. Since the thermoreflectance imaging requires close to normal incidence and collection of the reflecting signals, the NSOM probes were titled at 7º and 3º with respect to the object plane for imaging the tip region (~5-

100 μm) and the region far away from the tip (~100-500μm) respectively. Note that the thermoreflectance imaging at larger tilt angles (10-20°) corresponds to the region (0-5 μm) around the tip of the NSOM probe, where the taper angle changes sharply. The corresponding large change of the curvature as shown in Figure 5.3 causes main difficulty in the temperature measurement around the tip (within 0-5 μm) with thermoreflectance imaging. With high magnification optical setup additional noises of reflected signal due to large curvature around the tip [63] surpass the thermoreflectance signal and prevents the readable temperature measurement of the NSOM probe around the tip (within 0-5 μm). Similarly the end facet of NSOM probe cannot be imaged as the size of the end facet (<1 μm) is beyond the diffraction limit of the optical setup. For regions away from the tip (>5μm, refer to figure 5.3), the taper angle changes smoothly. The tilt angles 3˚ and 7˚ are the optimized angles we selected to measure the temperature of the specified NSOM probes to cover a region 5-80 μm and 150-350 μm away from the tip within an angle accuracy of $\pm$0.5°. Figure 5.3(b) illustrates the imaging configuration applied in the measurements. In order to image the region of NSOM probe where the tapering angle is ~7°, the probe was tilted by 7° with respect to the object plane. In this position, the top surface of the NSOM probe where the tapering angle is ~7° is parallel to the object plane and can be well focused. This tilting position provides the thermoreflectance image of NSOM probe within 5-100 μm measured from the tip. Similarly when NSOM probe is tilted by 3°, the thermoreflectance image of 100-500 μm region of the NSOM probe can be obtained. Figure 5.4 shows the optical image and thermoreflectance images of the NSOM probe for the two tilt angle settings used in the

experiments. The temperature plot of the NSOM probe from 5 to ~500 μm was obtained by combining the two thermoreflectance images with different tilt angles (Figure 5.4d). The shaded region in Figure 5.4d (i.e. 80-150 μm) shows those parts of NSOM probe which are slightly out of focus in the two tilt angle settings used in the experiments. The error induced by change of incident angle can be estimated by a simple relation as $angle^2/2$ for a wavy target within focus depth of optical/thermal imaging. For a surface with an monotonically increasing taper angle, the surface can eventually become out of the focus depth of imaging and causes even larger errors than that predicted with the simple relation during the temperature measurements with thermoreflectance [63]. As a result, the thermoreflectance imaging does not provide reliable temperature values at these regions. It is observed from Figure 5.4d that the main temperature increment of the NSOM probes is confined within <100 μm distance measured from the tip of the probe, which is well covered with the combined thermoreflectance imaging with two tilting angles for all the conditions studied.

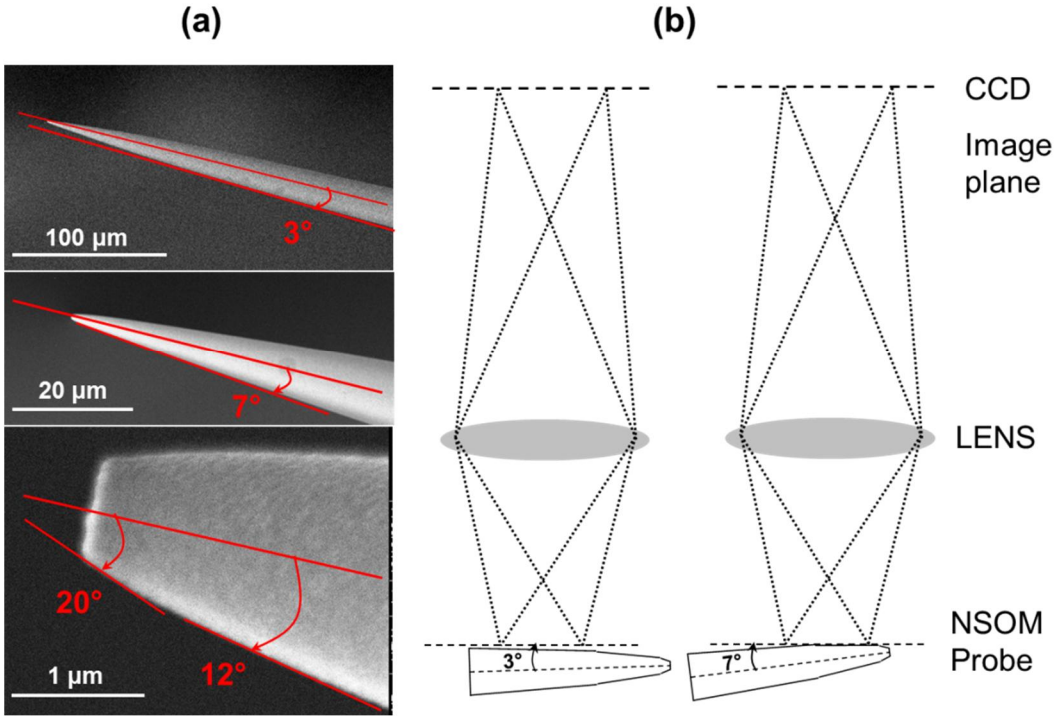

Figure 5.3: (a) SEM images of NSOM probe at different resolutions show the different taper angles along the NSOM probe, (b) illustrates the imaging configurations at the two tilt angles

The conversion between the change of the thermoreflectance of the gold coated NSOM probes to the temperature distribution of the probe is through thermoreflectance coefficient 'κ' of the gold coating of the NSOM probe. Documented 'κ' of bulk gold is ~-2.4x10^{-4} /K at 532 nm [69]. An in-house calibration of the thermoreflectance coefficient of ~200 nm Au film on a fused silica substrate (closer to the configuration of NSOM probes) shows that thermoreflectance of gold film varies linearly with temperature for temperature range 30°C-450°C with a calibrated 'κ' -3.97x10^{-4} /K. The related temperature from the thermoreflectance of NSOM probe with both published and

in-house calibrated values of 'κ' were considered in the results presented in following sections. The probing laser (i.e.532 nm) was selected as it has higher thermoreflectance response (i.e., change of reflectivity with respect to temperature) compared to other wavelengths (except ~490 nm) [69]. The probing laser power was at least three orders smaller than the pump laser used in this study to prevent the disturbance of the probe during the temperature measurement.

5.4 Results and Discussions

The heating of the NSOM probe is a strong function of the coupled light since the thermal process of the NSOM probe starts from the absorption of the incident optical energy at the metal coating of the probe and the resulting Joule heating. Lasers of different wavelengths, powers and the modulation frequencies can result in different heating behavior of the NSOM probe during the operation. In addition, the laser induced heating is affected by the configuration of the NSOM probes (e.g., the aperture size of the probe). In this study, four common variables in NSOM experiments that can affect the heating of the probes were examined, namely, (a) power, (b) modulation frequency and (c) the wavelength of the input laser along with (d) aperture sizes of the probe. The contribution of each factor on the heating of NSOM probes are discussed as follows.

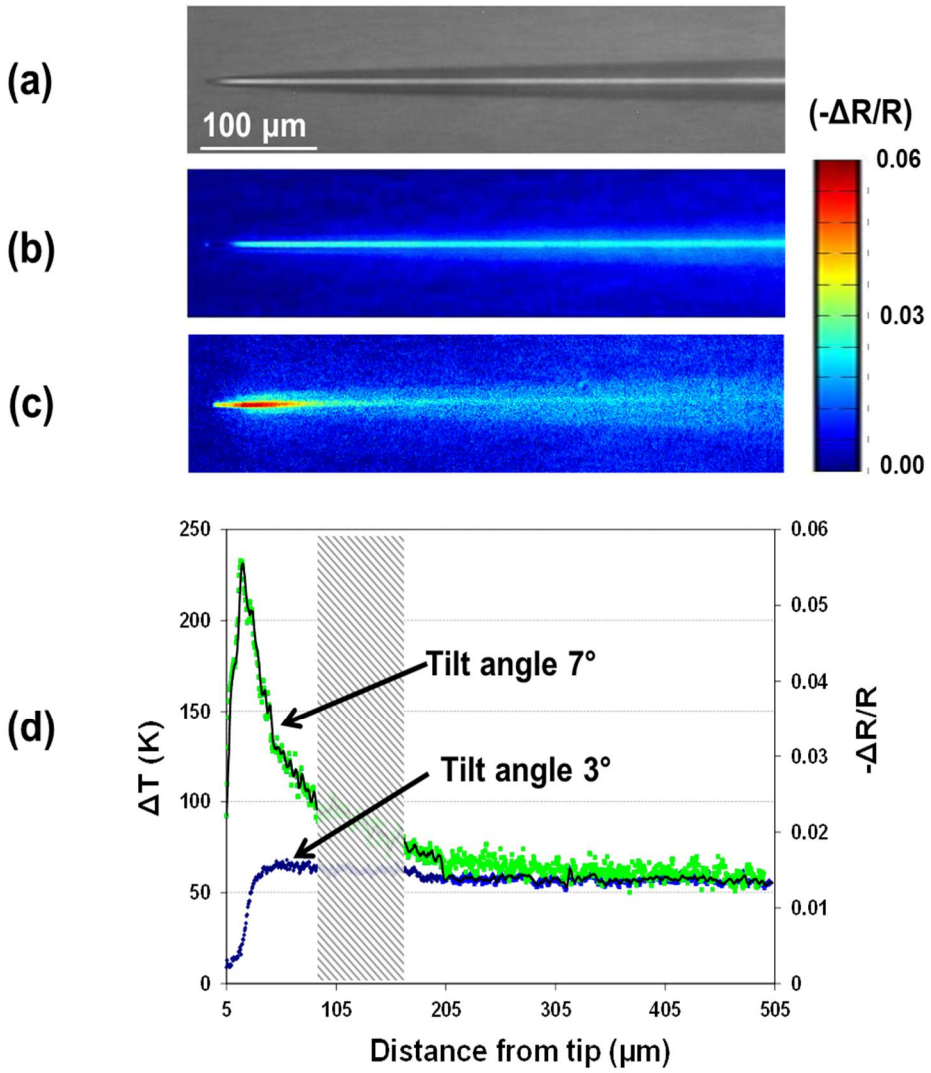

Figure 5.4: Optical and thermoreflectance images of NSOM probe in two different tilt positions a) optical image of NSOM probe, b) thermoreflectance image with ~3° tilt, c) thermoreflectance image with ~7° tilt, d) temperature plot obtained from combination of the two images. The corresponding temperature is calculated with $\kappa = -2.4 \times 10^{-4}$ */K. Within the shaded region, the surface deviates more than* ± 0.5 *from the normal direction during the thermoreflectance imaging and is out of the focus depth during the experiments*

A. Effect of input power of pump laser

To study the effect of laser power on temperature profile of NSOM probes, three laser powers (i.e. 0.3 mW, 0.6 mW and 1.2 mW) were used. A blue laser (405 nm) was selected as the pump laser considering the higher temperature induced by blue laser and the ease of temperature measurements. The pump laser was coupled to NSOM probe with 150 nm aperture (Figure 5.1). The modulation frequency of the pump laser was fixed at 0.5 Hz. It is observed in Figure 5.5 that the location of the peak temperature (~20-30 μm away from the tip) and the exponential decay trend of the NSOM probe temperature after the peak location are the same for the three examined laser powers. The peak temperature, however, varies almost linearly with respect to the input laser power. The linear temperature response with respect to the laser power suggests that convection and conduction are likely to be the dominant mechanisms of heat dissipation from the NSOM probe to the environment since both mechanisms have linear relationships between the dissipative power and temperature difference compared with thermal radiation [73]. The linear relationship may not be true at higher temperatures when thermal radiation dominates the conduction and convection however the probe may already be damaged at higher temperatures. From the obtained data, an empirical fit for estimating peak temperature for the given laser power is given by: $\Delta T = 600*P^2 - 86*P+82$, where P is power in mW. Note that the absolute temperature may be higher than the ΔT. Also this relation is applicable only for the 150 nm NSOM probe used in the current study.

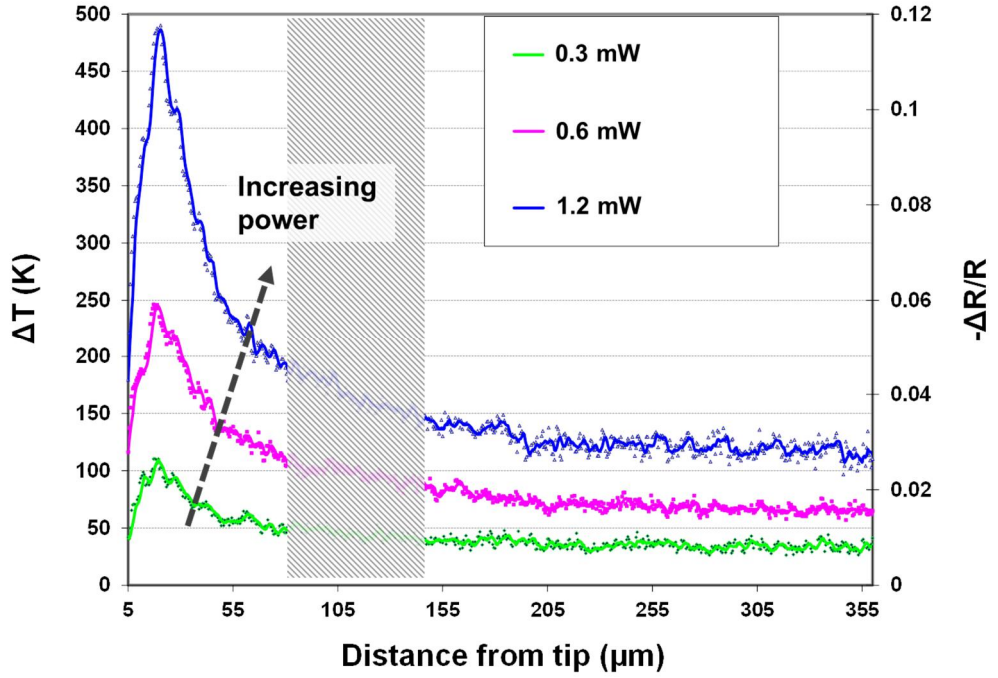

Figure 5.5: Temperature distribution along the NSOM probe under different laser powers

B. Effect of modulation frequency

To examine the contribution of the modulation frequency of the pump laser on the heating of NSOM probes, blue laser with laser input power 0.6 mW was coupled to NSOM probe with 150 nm aperture. Five modulation conditions namely, 0.5 Hz, 2 Hz, 4 Hz, 8 Hz and 16 Hz were examined (Figure 5.6). Figure 5.7a illustrates the effect of modulation frequency on the amplitude of the temperature of the NSOM probe between the laser on and off states. Note that laser is periodically turned on and off and it causes periodic heating of the NSOM probe during the homodyne thermoreflectance imaging of NSOM probes. When the modulation frequency increases, the amplitude of the resulting

modulated NSOM probe temperature decreases as the cooling rate of NSOM probe is closer to the modulating speed at higher frequency. As a result, stronger historic heating accumulates in the NSOM probe at higher modulation frequencies. On the other hand, for smaller modulation frequencies, the NSOM probe has enough time to dissipate its energy to the environment between two successive heating cycles. As a result, the maximum temperature (during laser on) and the minimum temperature (during laser off) of the NSOM probe can reach the quasi-steady-state values for very low modulation frequency. The similar trend between the NSOM probe heating and the modulation frequency of pump laser was observed in previous study with single point thermoreflectance [28]. When ΔT vs (2/modulation frequency) is plotted (Figure 5.7b), an exponential decay of the ΔT with respect to the cooling duration (2/modulation frequency) for different modulation frequencies is observed. An approximate value of time constant τ = 97 ms was obtained from fitting the exponential curve, which indicates the characteristic cooling time of the selected NSOM probe.

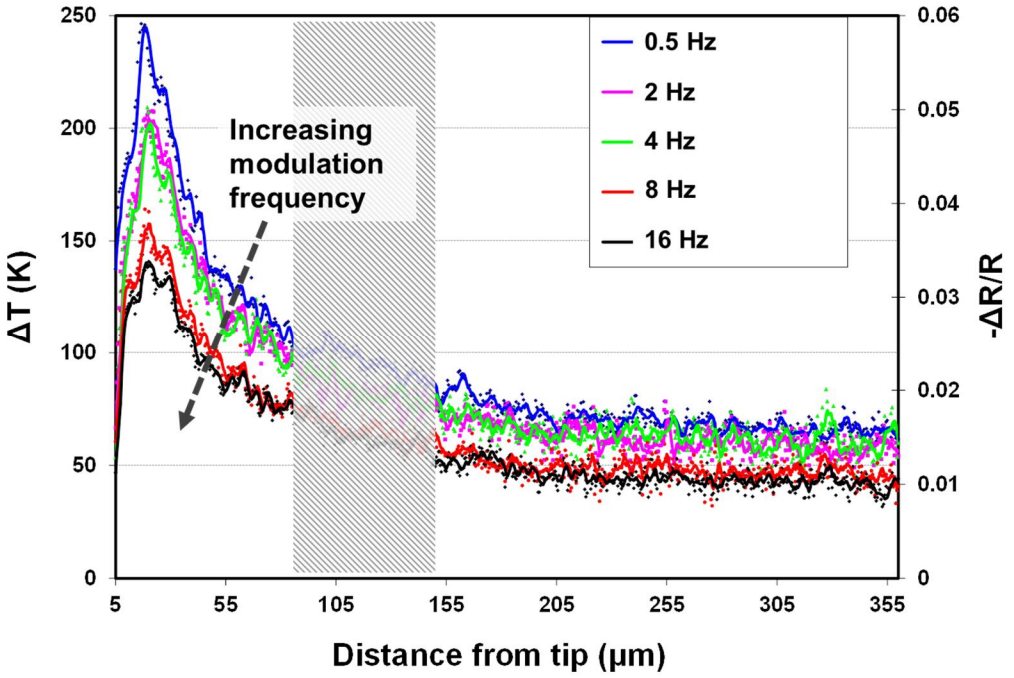

Figure 5.6: Temperature distribution along the NSOM probe under different modulation frequencies of pump laser

C. Effect of wavelength of pump laser

To study the effect of wavelength of pump lasers on the heating of NSOM probe, red laser (650 nm) and blue laser (405 nm) were selected as pump lasers. A straight NSOM probe with aperture 150 nm was coupled to pump laser (405 nm/650 nm) with laser power maintained at ~1.2mW. Figure 5.8 shows the temperature profile of NSOM probe

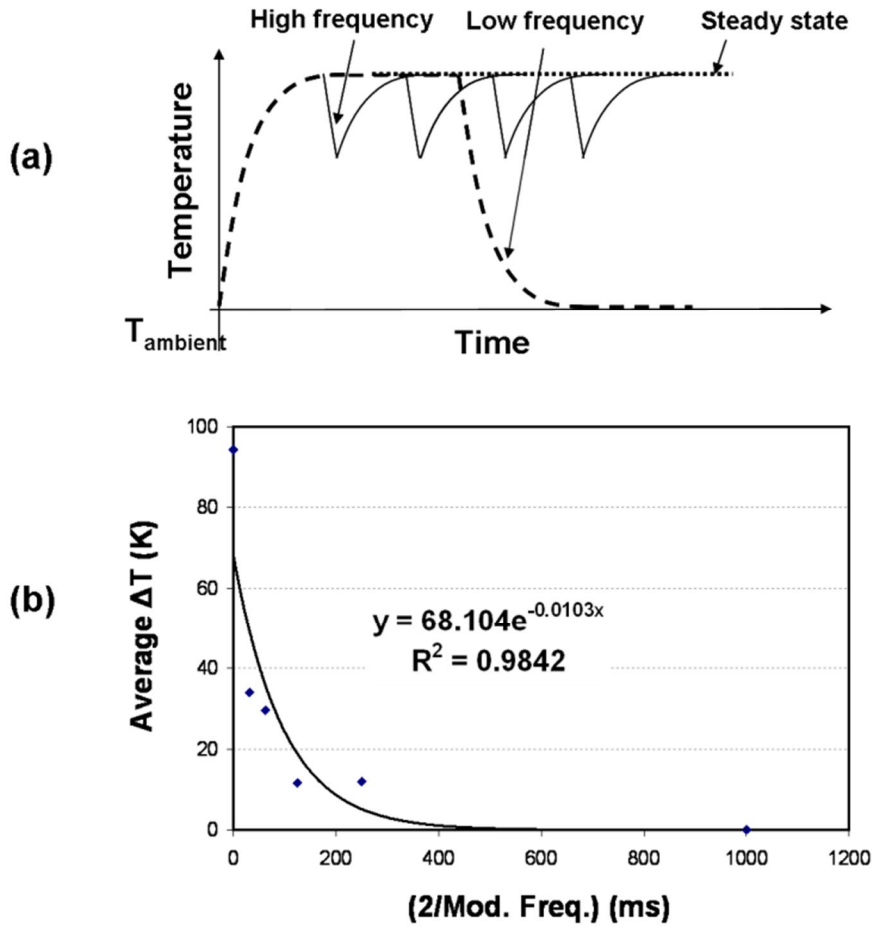

Figure 5.7: Effect of modulation frequency on the temperature response of NSOM probe; a) schematic diagram of the temperature response of NSOM probe with modulation frequency b) cooling curve obtained from the measured data

under the two wavelengths. The locations of hottest spot (i.e. peak temperature) is similar (i.e. 20-30 μm away from the tip) for both wavelengths. However, the peak values of temperature reached with the two wavelengths are significantly different. The peak temperature of the NSOM probe with blue laser is ~10 times higher than that with red laser under the same laser power.

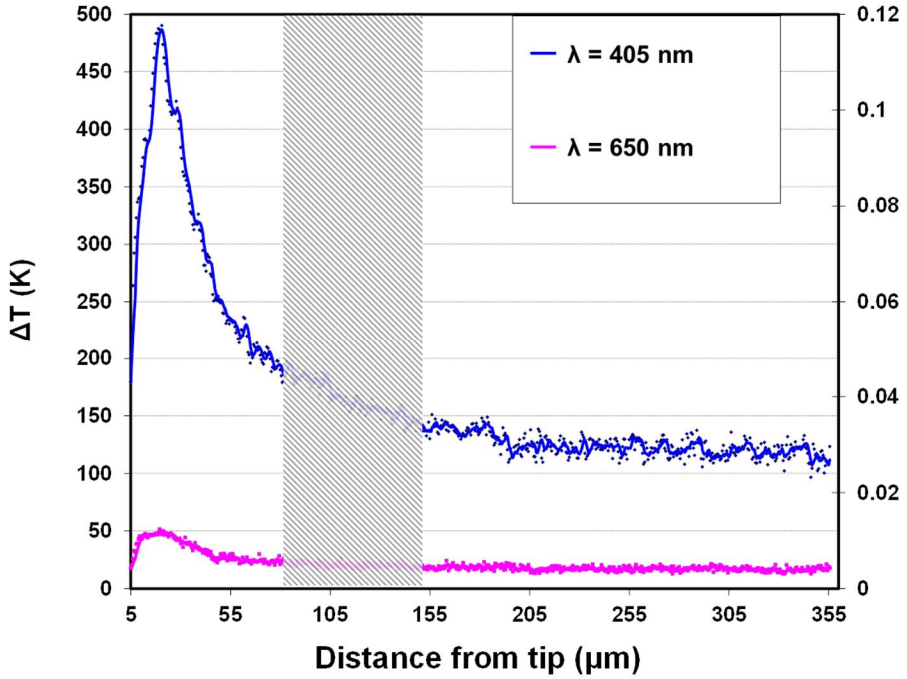

Figure 5.8: Temperature distribution along the NSOM probe under different laser wavelengths (i.e. 650nm and 405nm)

The significant difference in the heating behavior of NSOM probes for the two wavelengths can be understood from the dramatic change of light absorptivity of gold as a function of wavelength. The absorptivity of gold increases sharply when the wavelength is less than ~570 nm [74]. As a result, the gold film absorbs most of the incident blue light and causes a significant heating of the NSOM probe, while it reflects most of the red light and keeps the NSOM probe cool during the operation. To reduce the heating of NSOM probes with short wavelength lights (e.g., blue light), gold coating of NSOM probes may be replaced with a material with low absorptivity at shorter wavelengths (e.g., silver) [74].

D. Effect of aperture size of NSOM probe

To study the effect of aperture size on temperature profile of NSOM probe, two different NSOM probes with aperture size 150 nm and 250 nm were used. Both red and blue lasers were used as pump lasers for separate experiments. The input laser power (1.2 mW) and the modulation frequency (0.5Hz) were fixed in each experiment. The 150 nm probe is less than the diffraction limit of both blue and red lasers. However, the 250 nm probe is larger than the diffraction limit of the blue laser but less than the diffraction limit of the red laser. Figure 5.9 & 5.10 shows the temperature profiles of the two NSOM probes (i.e. 150 nm and 250 nm) operating under blue and red lasers respectively. The peak temperature is two times larger for 150 nm aperture NSOM probe than the 250 nm aperture NSOM probe when blue laser is applied (Figure 5.9). With red laser, aperture size shows much less effect on the probe heating: the NSOM probe with 150 nm aperture is only ~25% hotter than the NSOM probe with 250 nm aperture (Figure 5.10). The pronounced effect of aperture size on NSOM probe heating with blue laser can be attributed to the significant amount of light leakage from the higher-than-diffraction-limit aperture (i.e. 250 nm) which does not happen in the sub-diffraction-limit aperture (i.e. 150 nm). For experiment with red laser, both 150 nm and 250 nm apertures are less than the diffraction limit of the red light (>300 nm). Therefore, the change of the aperture size on the temperature of the NSOM probe with red laser is not as significant as that with the blue laser. Figure 5.9 and Figure 5.10 show a slight shift (~15 μm) in the location of peak temperature for the two NSOM probes used in the experiments. The diameter corresponding to the location of peak temperature for the 250

nm probe was 40% larger than that with the 150 nm probe (~7 μm) as observed in the SEM images of the two probes. The geometric shape (i.e. taper angle) of the probe changes among probes with different apertures due to difference in parameters in a programmable fiber puller for preparing tapered NSOM probes [8]. This may be one of the reasons of the shift in location of peak temperature with the two probes with different apertures. For probes with the same apertures, the obtained straight probes from Nanonics Imaging Ltd. showed good consistency in terms of the geometry based on the SEM images taken before the experiment. Note that the temperature profile obtained from thermoreflectance measurement showing a hottest region about 20-50 μm away from the tip is true for the selected NSOM probes with small tapering angle and gold coating used in this study. For other NSOM probes with different tapering angle, aperture size, and coating material (e.g., highly reflective silver and aluminum), the position of the hot spot along with multiple hot spots appearing closer to the tip may occur during the operation [21, 22, 27].

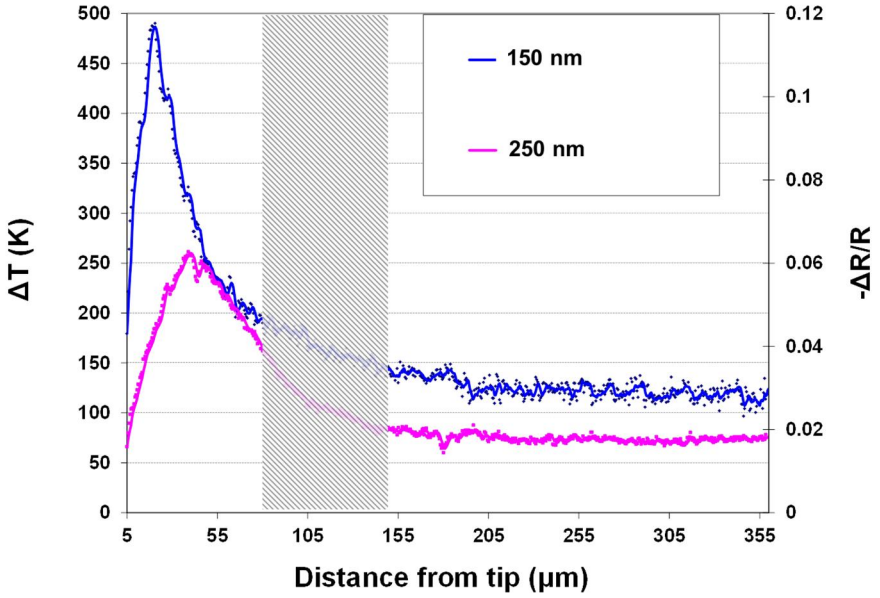

Figure 5.9: Temperature distribution along the two different NSOM probes (i.e. 150 nm and 250 nm aperture sizes) under blue laser as pump laser

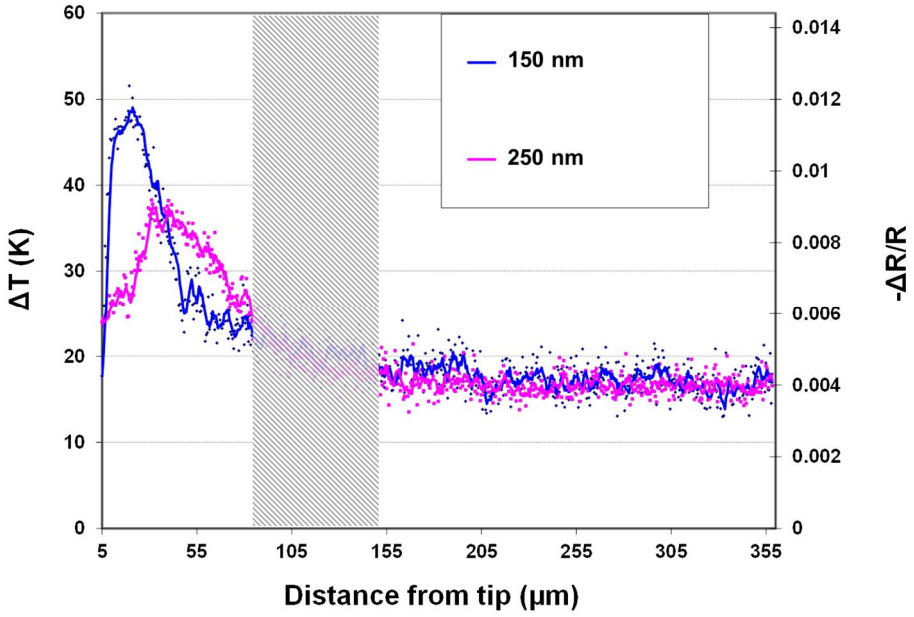

Figure 5.10: Temperature distribution along the two different NSOM probes (i.e. 150 nm and 250 nm aperture sizes) under red laser as pump laser

It was found in the experiments that the gold coating of the NSOM probes showed a decay in its quality under long term operation at higher operating laser powers (e.g., ~2-3 mW for blue laser). Figure 5.11 shows the SEM images of NSOM probe after the experiments with high laser powers (~2-3 mW). Nano-craters were observed all over the region close to the tip (~50 µm). The nano-craters could be induced by the thermal stresses occurring during the strong cyclic heating of NSOM probes during the experiments. Also, a damaged tip can be observed in the SEM image (Figure 5.11) which can be due to high temperatures (close to the melting temperature of gold coating) reached during the experiments.

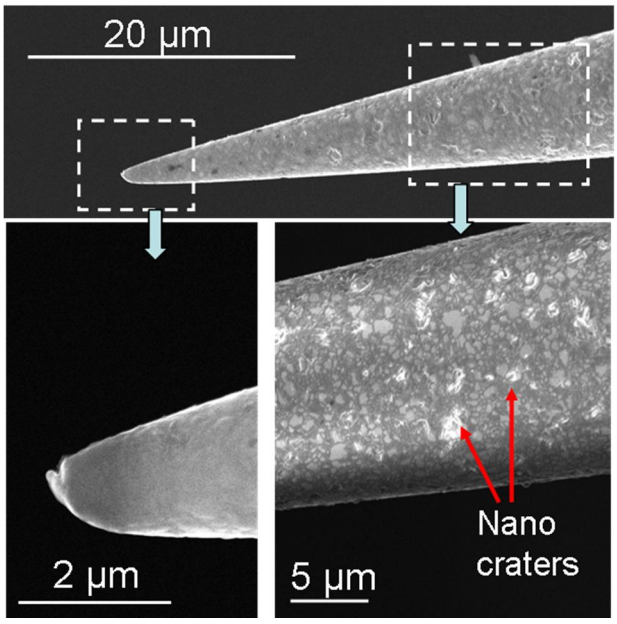

Figure 5.11: SEM images of the NSOM probe after high power experiments shows nano-craters on the surface along with melting of the tip

5.5 Summary

The contributions of power, modulation frequency and wavelength of the pump laser along with the aperture size of NSOM probes on the heating of NSOM probes were studied with non-intrusive 2D thermoreflectance imaging. The measurement indicated strong heating at ~20-30 μm away from the tip. The change in wavelength of input laser shows no significant effect on the location of the hottest spot. However, the temperature of NSOM probes is dramatically different for the two wavelengths of pump laser selected in this study. The blue light (405 nm) provides significant heating of NSOM probes compared with red light (650 nm). For each wavelength, the temperature of the NSOM probe varies almost linearly with the input laser power. The modulation frequency of pump laser to the NSOM probe also shows contributions to probe heating. It was observed that the fluctuation of temperature during periodic heating decreases with higher modulation frequency of input light. In addition, the aperture size of NSOM probe is another parameter that can affect its heating during operation. NSOM probes with sub-diffraction-limit aperture can result in stronger heating of the NSOM probe than that of higher-than-diffraction-limit aperture since the large aperture size allows pump laser to leak from the aperture and reduces heating during operation.

The possible thermal expansion of the NSOM probe was not observed in the current experimental set-up which has a spatial resolution limited with far field optical imaging (i.e. >1 μm). However, bending of the NSOM probe can be clearly observed during the laser heating when the geometry of the NSOM probe is not axisymmetric (e.g., cantilevered NSOM probes). Therefore, to prevent the unwilling direct contact and the

resulting mechanical damage of NSOM probes under higher laser intensities, straight NSOM probes can be a better choice than the cantilevered NSOM probes. Note that the developed thermoreflectance imaging can only resolve the regions larger than ~5 μm from the tip of the probe. For regions between 0 to 5 μm from the tip of the probes, alternative methods such as finite element analysis will be required to determine the temperature profile. The developed 2D thermoreflectance imaging can be further extended to have nanosecond (ns) time resolution for transient heating of NSOM probes when the continuous laser is replaced with ns pulsed laser. The study of the transient thermal response of NSOM probes with the newly developed ns time resolved TR is presented in the following chapter 6.

6. NANOSECOND TIME RESOLVED THERMOREFELCTANCE IMAGING WITH COHERENCE CONTROL OF LASER PULSES*

6.1 Introduction

To extend the temporal resolution of 2D thermoreflectance imaging, which is typically in μs to ms range, to nanosecond (ns) level, ns pulsed light with high enough intensity is required in the generation of TR images [75-77]. Nowadays, high intensity laser can provide intense light with femtosecond or even attosecond pulse duration. The laser light, due to the stimulated emission, is spatially and temporally coherent. The highly coherent light is undesired in optical imaging because of the formation of speckles (high-contrast fine-scale granular pattern) and large fringe patterns [70, 78-80] which ruin the imaging features of the target. To eliminate the formation of speckles and large fringe patterns in a time-domain thermoreflectance (TDTR) imaging with lasers, the relationships between the speckles and large fringe patterns with the temporal and spatial coherence of laser light should be identified and controlled. It is found that large fringe patterns are mainly attributed to the high spatial coherence (statistical similarity over large coherence area) of reflected light from smooth patterns on a substrate. Small stationary speckle patterns, on the other hand, are mainly attributed to the high temporal coherence (statistical similarity over time) of the illumination light which provides less variation of phases and results non-uniform illumination [72, 80]. Both interference

*Reprinted with permission from "A methodology for nanosecond (or better) time resolved thermoreflectance imaging with coherence control of laser pulses" by Soni A., Sundaram V. M., Wen S. B., 2013, Appl. Phys. Lett. 102, 203112, Copyright 2013 by American Institute of Physics

patterns are undesired and cause noise signal which can easily overwhelm the temperature information carried in the reflected light. Traditional techniques in reducing the coherence of light include moving diffusers, fiber bundle with varying length fibers and moving mirrors in a continuous wave (CW) laser illumination, which provides destruction of spatial coherence and increased fluctuations of phase with time [70, 72]. Unfortunately, these techniques suffer from low response time (ms) and cannot be directly applied in fast TDTR requiring ns response.

In this study, the reduction of temporal coherence is achieved by spectral broadening of the pulsed laser in a non-linear medium [81]. The reduction of spatial coherence is achieved by sending light through an optical fiber bundle with variation of lengths to induce spatial angular diversity [72]. Quantitatively, the level of coherence reduction required to achieve desired contrast in interference patterns in an imaging system can be estimated using the reduction factors due to wavelength and angular diversities [80, 82].

6.2 Experimental Setup

To validate the above idea, a laser based ns-TDTR imaging system with reduced light coherences is developed in this study (Figure 6.1). An Nd:YAG laser operating at second harmonic (λ~532 nm) with E~60 mJ is adopted as the probe light. To suppress the temporal coherence, the probe light is first delivered to a glass cell filled with CS_2 liquid [81] to achieve a spectral broadening of ~0.2 nm which increases the wavelength diversity factor by ~6 times (original spectral width of laser ~0.03 nm). To suppress the spatial coherence, this probe light is further delivered to a fiber bundle composed with

~7000 multimode fibers which provides effective angular diversity factor >80 [82]. The combined reduction factor in the intensity contrasts of the interference patterns is ~500 which provide speckle-free and large fringe patterns free images in the TDTR imaging.

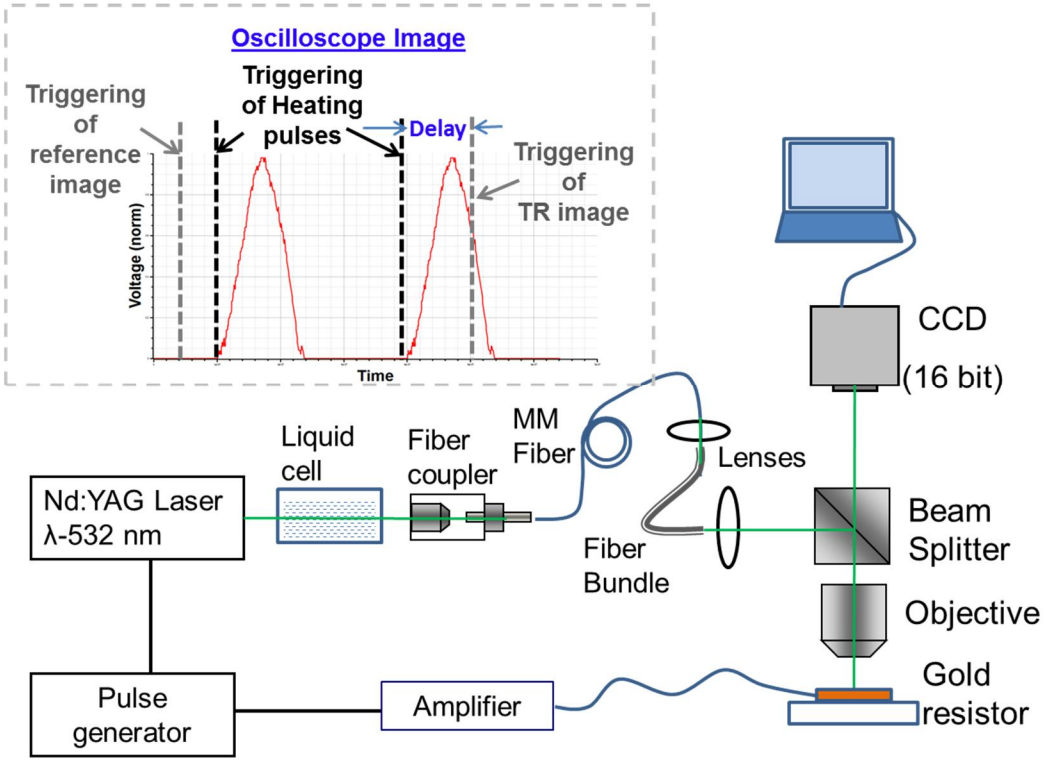

Figure 6.1: Schematic of the experimental setup for nanosecond time-resolved thermoreflectance imaging

To obtain a fixed spatial intensity profile of the probe light, a multimode-fiber acting as a spatial mode filter is inserted between the fiber bundle and CS_2 liquid cell during the experiments. The probe light with reduced temporal and spatial coherences is collimated and projected on the target through non-polarizing beam splitter and an

objective lens as in Figure 6.1. The reflected images are captured by a CCD camera (Opteon, 120 fr/sec, 16 bit, B/W). A gold resistor (8 μm × 40 μm with 100 nm thickness, Figure 6.2) fabricated on a thick quartz plate is selected as a transient heating target to be examined with the developed ns-TDTR imaging. The gold resistor is heated with pulsed signals gated with a pulse/delay generator (Berkeley Nucleonics 575 pulse/delay generator). Two images are captured for each pulsed heating of the resistor: reference image is captured before the electric pulse and the TR image is captured at a fixed delay time with respect to the electric pulse (as shown in the oscilloscope image of Figure 6.1). The two images are subtracted to obtain the change of the thermoreflectance profile at a given delay time. Measurements are repeated ~6400 times to achieve ~1 K temperature resolution from the averaged results [68]. The temporal resolution of the developed ns-TDTR imaging is determined by the pulse duration of the probe light (~4 ns in this study). Higher temporal resolution can be achieved when the ns probe light is replaced with ps probe light in the future. The spatial resolution of the imaging setup is ~1.1 μm, limited by the digital resolution based on the effective NA 0.29, 10 X magnification and CCD pixel size ~5.5 μm.

6.3 Simulation

The pulsed heating of fabricated gold resistor was simulated with FEM method in commercial software (COMSOL 4.2a). To replicate the 3D geometry of the fabricated resistor the length and width of the resistor was obtained from SEM image and the thickness was measured using an AFM system (Veeco Inc.). The voltage pulse from pulse generator followed by the homemade amplifier was measured with an

oscilloscope. Figure 6.2 shows the 3D model of the gold resistor on quart substrate. The simulation solves the transient heat diffusion equation with heat source from Joule heating. Bulk properties (i.e. thermal conductivity, electrical conductivity, specific heat and density) for gold and quartz substrate. The temperature profiles at different times during and after the electric pulse were recorded and plotted in SciDAVis along with the measured results for comparison.

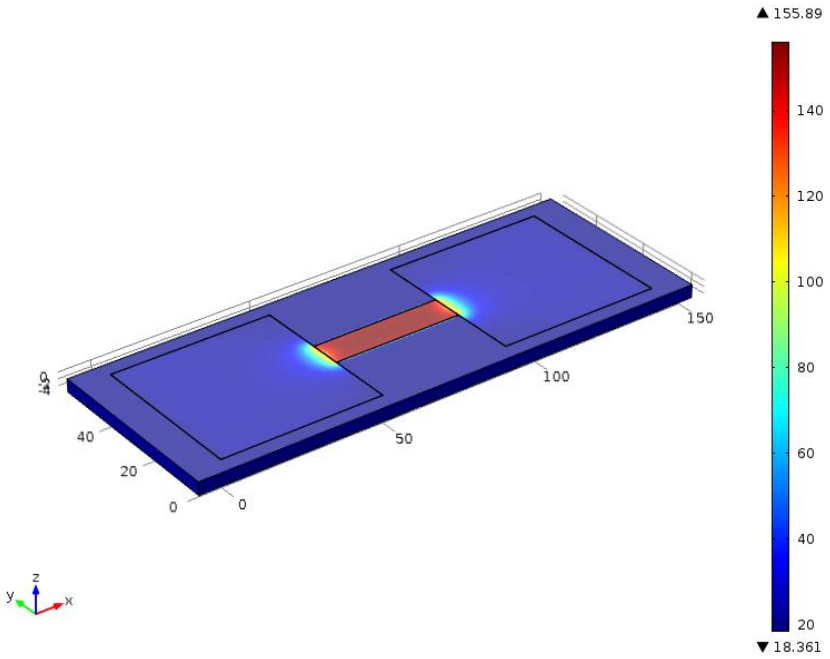

Figure 6.2: 3D model of gold resistor and quartz substrate and temperature distribution after the pulsed heating

6.4 Results and Discussions

Qualities of the reflected images of the micro gold resistor when the probe light from the laser strikes the resistor (a) after passing through optical fiber bundle only, (b)

after passing through CS2 liquid only and (c) after passing through the CS_2 liquid followed by optical fiber bundle are illustrated in Figure 6.3. When the temporal coherence of the laser light is reduced with spectral broadening in the CS_2 liquid, the speckle patterns are suppressed but large fringe pattern are still observed due to spatial coherence. When the spatial coherence of the laser light is also reduced by further delivering the light through an optical fiber bundle, the large interference patterns are also suppressed. The resulting optical image (Figure 6.3c) is speckle-free with no large interference patterns and fixed spatial intensity distribution. This high quality optical image is the basis for the success of ns-TDTR imaging in this study (Figure 6.3d).

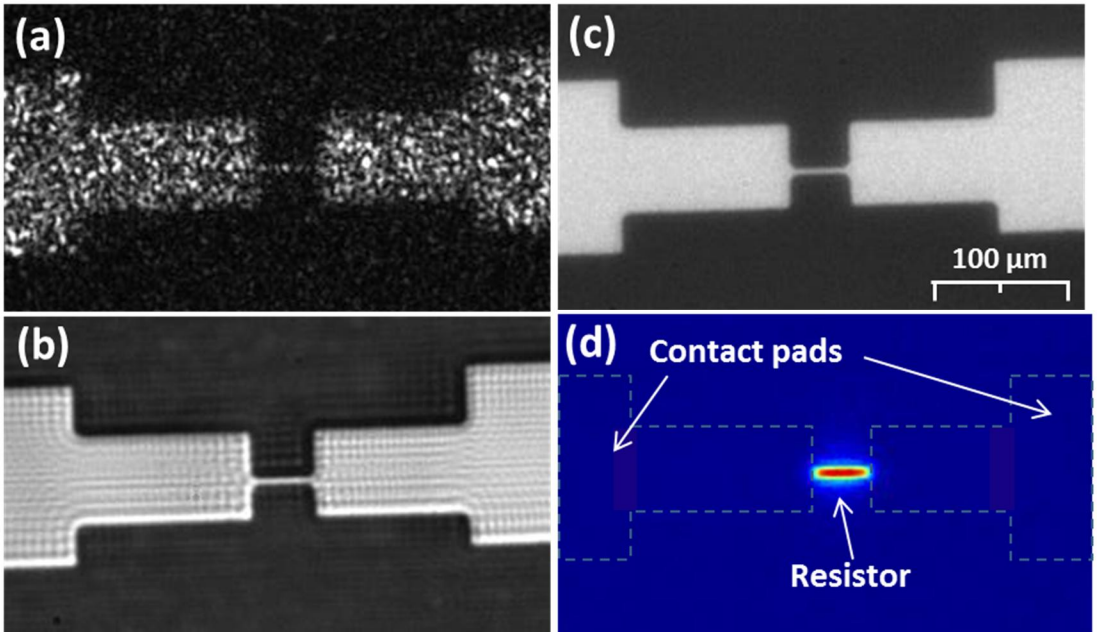

Figure 6.3: Quality of optical images a) without spectral broadening, b) without angular diversity from the fiber bundle, c) with spectral broadening and angular diversity from the fiber bundle and d) resulting TR image

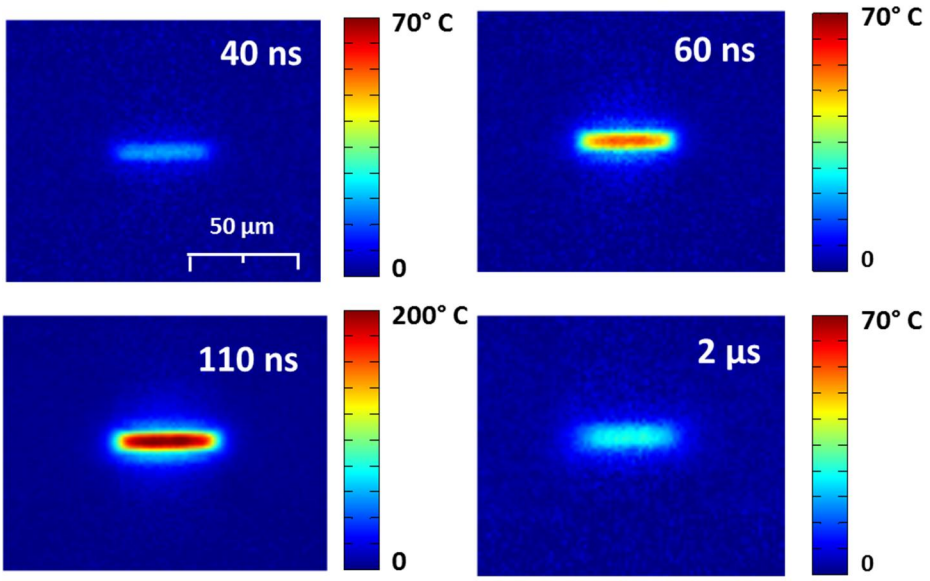

Figure 6.4: 2D thermoreflectance (TR) profiles on gold resistor at different delay times

To examine the validity of the ns-TDTR, the 2D thermoreflectance profiles of a gold resistor under ~110 ns pulsed heating is recorded at different delay times (Figure 6.4). A lab calibrated thermoreflectance coefficient -2.4×10^{-4} K^{-1} [64, 69] is used to convert the TR data to temperature profiles (Figure 6.5 and 6.6). The resulting spatial and temporal temperature profiles and the corresponding numerical results of gold resistor are illustrated in Figure 6.5 and 6.6. The deviation between the measured and predicted spatial temperature profiles (Figure 6.5) can be attributed to the fabrication defects in the geometry of the gold resistor, which are not considered in the numerical simulation. The deviation between the experimental and theoretical values in the temporal response (Figure 6.6) can be attributed to the parasitic capacitance/inductance of the heating circuit/elements, geometric effects on electrical/thermal conductivity, and

the contact resistance between the resistor and substrate [83], which are not included in the numerical simulation.

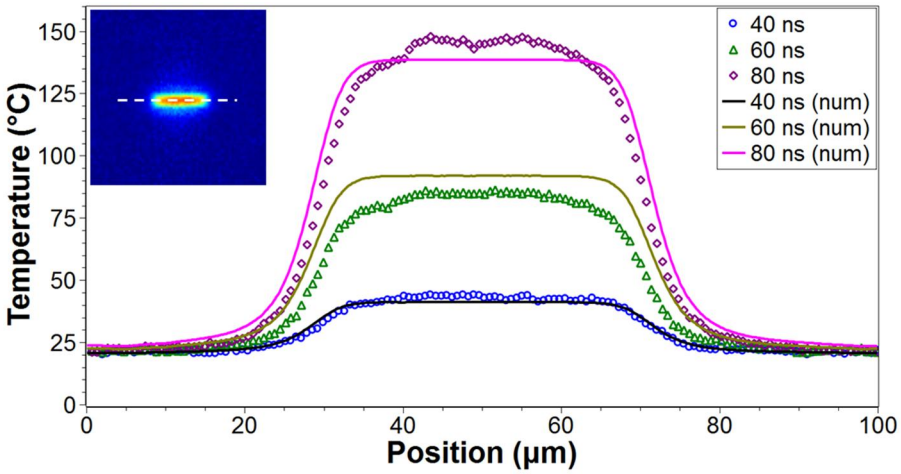

Figure 6.5: Spatial temperature profile at various delay times from TR measurements (in symbols) and from numerical simulation (in solid lines)

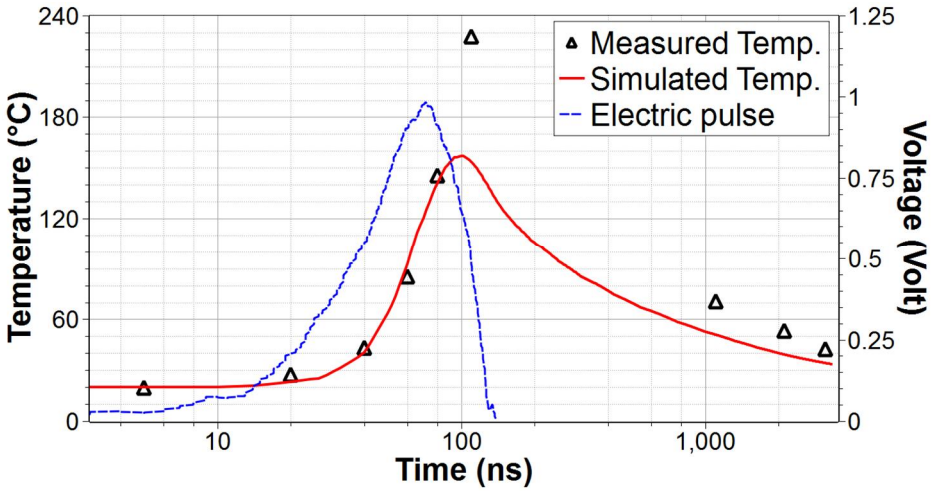

Figure 6.6: Temporal evolution of temperature at central spot of gold resistor from TR measurement (in symbol) and numerical simulation (in solid line). Dashed blue line shows the electric pulse

6.5 Temperature Evolution of NSOM Probe under Pulsed Operation

The ns-TDTR setup was further modified for temperature measurement of NSOM probe under the nanosecond pulsed operation. The modified ns-TDTR setup includes the nanosecond pumping of NSOM probe with nanosecond (OPOTek) laser providing ~4 ns laser pulses to NSOM probe, the x-y translation and tilting stage for controlling the position and tilt of NSOM probe during thermoreflectance imaging (Figure 6.7). The pump and probe laser were synchronized with the CCD camera with the delay generator. The pulse energy ~2nJ was delivered to the NSOM probe and thermoreflectance images were recorded for delay time 0 to 50 ns with respect to the pumping laser. Figure 6.8 shows the temperature evolution of the NSOM probe at different delay times.

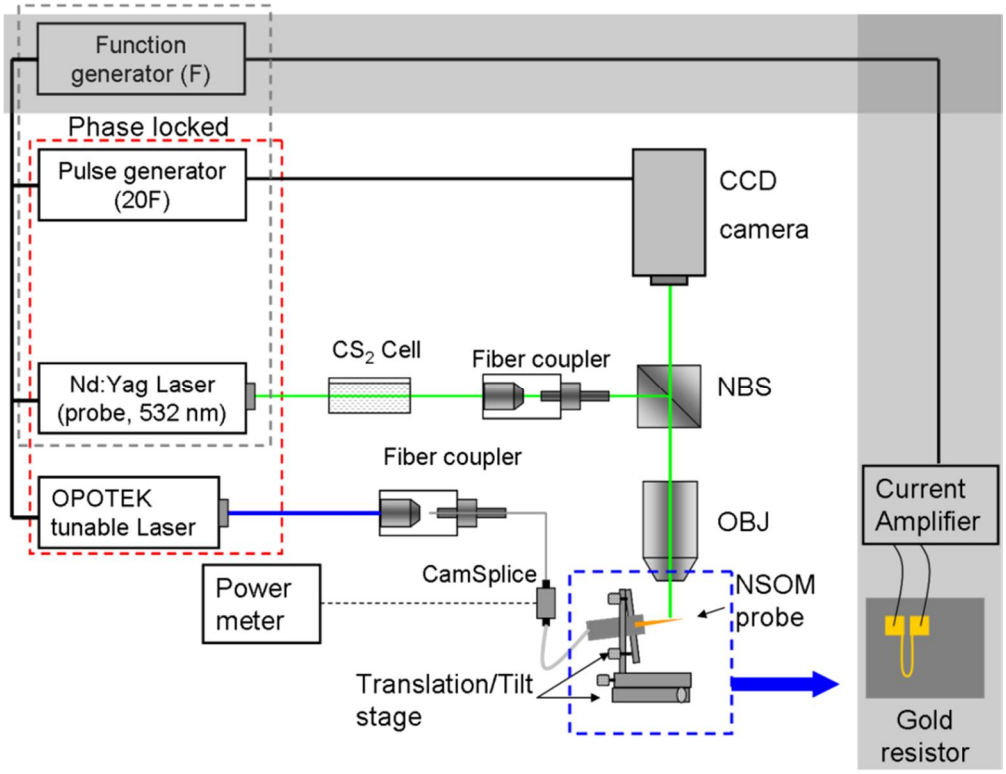

Figure 6.7: Modified TDTR setup for TR imaging of NSOM probe. Shaded area corresponds to the experimental configuration for gold resistor

As observed in the Figure 6.8, the location of peak temperature is close to the tip and the entire heating region is ~100 µm. Compared to the quasi-steady state operation as studies in last chapter the peak temperature occurs closer to the tip. This can be understood from the competition between the heat generation and heat dissipative rate at different location along the NSOM probe: at the tip location with strongest joule heating per unit volume. As a result, the tip experiences the highest temperature during pulsed heating when the pulse duration is short and the entire heating processes is also adiabatic. In addition, to the strong heating, the tip also experiences highest heat

dissipation rate due to its large surface-to-volume ratio. This strong heat dissipation is expected to overcome the strong heat generation at the tip under quasi-steady state heating. As a result, the quasi-equilibrium temperature of the tip is lower than the region close to ~20 μm location from tip under continuous laser pulse. As the time progresses the energy is dissipated toward larger heat capacity regions (i.e. bulk fiber).

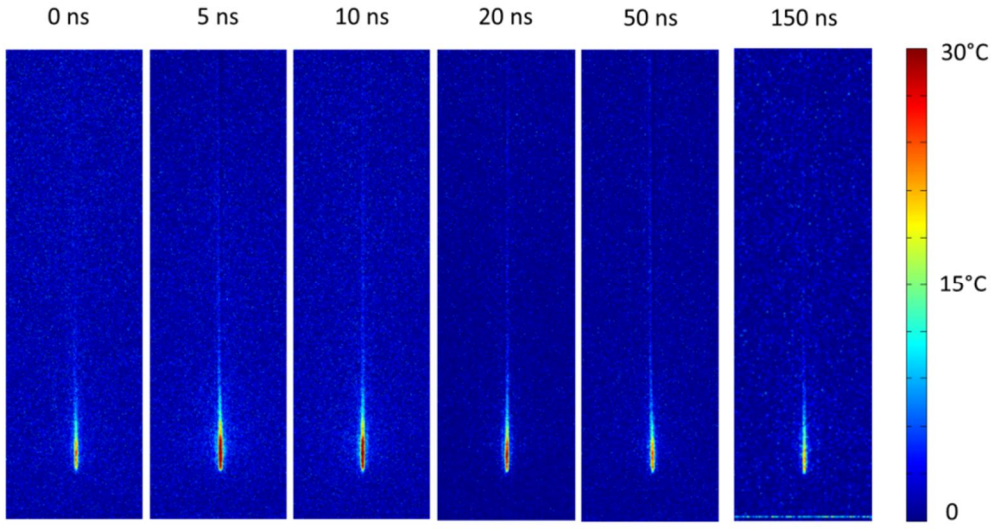

Figure 6.8: TR images of NSOM probe at different delay times under pulsed heating

6.6 Summary

In conclusion, a new methodology of ns-TDTR imaging allowing ns (or even ps) time resolution with diffraction limited spatial resolution is proposed and demonstrated in this study. Coherent pulsed laser is selected as the illumination source to achieve the required temporal resolution. Parasitic interference patterns, which are the main obstacles in applying laser in optical imaging, are diminished through identifying their

origins. Methods demonstrated in this study to reduce spatial and temporal coherence of pulse light without changing the pulse duration are spectral broadening in non-linear media and increased angular diversity with optical fiber bundle, respectively. The effectiveness of the developed ns-TDTR imaging is validated with the temperature measurement of a micro gold resistor under ~110 ns pulsed heating. The same methodology can be applied for ps time resolution TDTR measurements when a ps laser is applied.

This new time resolved thermoreflectance method is also applied to study the transient heating of NSOM probes. It is observed that the transient temperature profile of the NSOM probe is entirely different from the quasi-steady-state.. This temperature measurement also explanation the causes of the differences in the location and type of thermal damage of NSOM probes as a function of laser pulse duration (Figure 3.7 and Figure 5.11). The developed new methodology is valuable in the non-contact study of energy transport, defect detection and property characterization in microelectronic and photonic devices under pulsed or high frequency heating (e.g. with ultrafast lasers).

7. CONCLUSIONS AND FUTURE WORK

7.1 Conclusions

Laser machining is a popular fabrication method owing to the cleanliness, fast speed and higher precision compared to other fabrication processes. Compared to other nano-fabrication methods such as Focused ion beam, x-ray lithography, e-beam lithography laser fabrication can be conducted in a background gas which makes it more cost effective compared with other nano-fabrication processes. The spatial resolution of traditional laser fabrication is limited due to the application of far-field optics. In past few decades there is a demand for novel nano-fabrication methods and laser matching can be a potential method. The development of nano-optics devices enabled us to achieve deep sub-wavelength resolution. With the use of nano-optic devices there is a high potential to apply laser machining for nano-fabrication. However the poor light transport efficiency and associated thermal damage are the main challenges in applying nano-optics devices for laser nano-machining. The possibility of laser nano-machining with a commercial nano-optic device (i.e. near-field optical microscope (NSOM) probe) was explored in this research. The nano-pattern formation mechanism with a NSOM probe and pulsed lasers on different target material was studied through experiments. To understand the heating effects in NSOM probe, thermoreflectance imaging was adopted for measuring the temperature of NSOM probe under operation. To extend the thermoreflectance measurement to pulsed operation of NSOM probe a novel method was developed to achieve nanosecond time resolved thermoreflectance imaging.

In the first part of the research, nano-patterns were generated with a pulsed laser (ns/fs) along with a commercial NSOM system. A systematic study was conducted to understand the size and shape of nano-patterns generated on selected semiconducting (Si & Ge) and metallic (Cr, Cu and Ag) targets under different laser pulse durations, laser energies and number of laser pulses. Based on the experimental results, femtosecond laser pulses, compared with nanosecond laser pulses, provide lower damage thresholds to the targets but higher damage thresholds to the NSOM probes at the wavelength (~400-410 nm) studied. Furthermore, the resulting nano-patterns showed a significant dependence on the optical properties (i.e., absorption coefficient and surface reflectivity) of the target material. By comparing the obtained experimental results, we conclude that the optical energy transport from the NSOM probe to the target dominates the pattern generation when femtosecond laser is applied to the NSOM system. When nanosecond laser is applied, both the thermal and optical energy transported from the NSOM probe to the targets attribute to the obtained morphology of nano-patterns on different targets under the experimental conditions studied.

To further understand the morphology and chemical composition of nano-patterns on silicon under nanosecond pulses, which showed deviation from the femtosecond results, a detailed examination of the nano-patterns was conducted through chemical analysis with EDS and XPS and then the nano-patterns were cut with FIB and observed under TEM. Compared with previous experimental results with femtosecond laser, nano-patterns in a format of protrusion generated under this new combination cannot be understood with surface oxidation and ablation (appeared in previous fs

experiments). Instead, the nano-patterns were generated through nanoscale melting and recrystallization when nanosecond laser pulses were applied. These nano-protrusions were composed with SiO_2 and nano-crystallized Si (nc-Si). The concentration of nc-Si in the nano-protursions showed a dependence on background gas studied (i.e., air and Ar).

From the above studies, it is concluded that light induced heating and subsequent damage of NSOM probe is the main limitation in adopting NSOM probe as a tool for nano-machining. NSOM probes can be easily damaged under moderate intensity laser pulses even before generating any pattern on the target. The second part of this research was focused on estimating the heating effects in NSOM probes under operation. A nonintrusive optical measurement technique (i.e., thermoreflectance method) was adopted to study the light induced heating of near field scanning optical microscope (NSOM) probes. The thermoreflectance measurements indicate that there is a hot spot at 20-30 μm away from the tip of the probe. The location of the hot spot is not a strong function of laser wavelength for a fixed type of NSOM probe. The temperature of the NSOM probes increases almost linearly with respect to the input laser power. The shorter wavelength light (405 nm) provides stronger heating of gold coated NSOM probes compared with longer wavelength light (650 nm). The modulation rate of the input laser also shows contribution to the heating of the NSOM probes: the temperature variation of NSOM probes decreases with increase in the modulation frequency of the input light. In addition to laser conditions, the NSOM probe with smaller apertures suffers stronger heating compared with that of larger aperture.

The laser machining usually applies a short pulsed laser as heating source due to the smaller heat affected zone which provides better spatial resolution and high precision in laser machining. To extend the energy transport analysis with thermoreflectance imaging of nano-optic devices it is necessary to increase the time-resolution of TR imaging to nanosecond or picosecond level. In the last part of the research, a time-domain thermoreflectance imaging (TDTR) methodology with pulsed laser illumination was developed to achieve nanosecond time resolution with diffraction limited spatial resolution. Validation of the proposed new methodology through a transient temperature measurement of a micro gold resistor under ~110 ns pulsed heating was demonstrated, which shows consistency with the corresponding numerical simulation. The new approach allows us to determine of the transient energy transport in miniature structures such as microelectronic and nano-photonic devices. This newly developed setup was used to determine the temperature profile of NSOM probe under nanosecond pulsed operation which showed difference in temperature profile compared with the quasi-steady state operation. From the observed results it was concluded that due to the short pulse duration under nanosecond pulsed operation, the heat generation rates overpowers the heat dissipation rate and provides much more confined heating closer to the tip. Under quasi-steady state operation the heat dissipation rate catches up with the heat generation rate and provides much large heated region.

7.2 Future Work

The current study can be extended for the energy transport study of new nano-optics and plasmonic devices. It was concluded from this research that the existing

NSOM probes need further modifications in the geometry (e.g. larger taper angle) to provide higher transport efficiency with minimized heating effects. This study can be extended to modify the design of NSOM probes or develop new types of NSOM probes with varying geometry. To precisely construct a more robust NSOM probe for laser machining the following factors should be studied in the future.

i. Effect of taper angle on light transport efficiency and higher damage threshold of NSOM probes.
ii. In situ measurement of output of NSOM probe and estimation of optical and thermal energy transport from NSOM probe to the target.
iii. Deep UV transient thermoreflectance imaging with a spatial resolution of 100-200 nm.

REFERENCES

[1] A. E. Siegman, *Lasers*. Mill Valley, Calif.: University Science Books, 1986.

[2] K. F. Renk, *Basics of laser physics : for students of science and engineering*. New York: Springer, 2012.

[3] A. C. Eckbreth, *Laser diagnostics for combustion temperature and species*. Tunbridge Wells, Kent ; Cambridge, Mass.: Abacus Press, 1988.

[4] A. Boutier, *Laser velocimetry in fluid mechanics*. London Hoboken, NJ: ISTE Ltd. ; John Wiley & Sons, 2012.

[5] P. Schaaf, *Laser processing of materials : fundamentals, applications and developments*. New York: Springer, 2010.

[6] K. Thyagarajan and A. K. Ghatak, *Lasers : fundamentals and applications*, 2nd ed. New York: Springer, 2010.

[7] W. G. Roeterdink, L. B. F. Juurlink, O. P. H. Vaughan, J. D. Diez, M. Bonn, and A. W. Kleyn, "Coulomb explosion in femtosecond laser ablation of Si(111)," *Applied Physics Letters*, vol. 82, pp. 4190-4192, Jun 9 2003.

[8] *Terminology for nanoscale measurement and instrumentation* vol. PAS 133. UK: British Standards, 2007.

[9] E. Betzig and J. K. Trautman, "Near-Field Optics - Microscopy, Spectroscopy, and Surface Modification Beyond the Diffraction Limit," *Science*, vol. 257, pp. 189-195, Jul 10 1992.

[10] L. Novotny and B. Hecht, *Principles of nano-optics*. Cambridge ; New York: Cambridge University Press, 2006.

[11] E. Betzig, J. K. Trautman, T. D. Harris, J. S. Weiner, and R. L. Kostelak, "Breaking the Diffraction Barrier - Optical Microscopy on a Nanometric Scale," *Science*, vol. 251, pp. 1468-1470, Mar 22 1991.

[12] E. H. Synge, "A suggested method for extending microscopic resolution into the ultra-microscopic region.," *Philosophical Magazine*, vol. 6, pp. 356-362, Aug 1928.

[13] L. Novotny, "The history of near-field optics," *Progress in Optics, Vol 50*, vol. 50, pp. 137-184, 2007.

[14] A. H. Larosa, B. I. Yakobson, and H. D. Hallen, "Origins and Effects of Thermal-Processes on near-Field Optical Probes," *Applied Physics Letters*, vol. 67, pp. 2597-2599, Oct 30 1995.

[15] B. I. Yakobson, A. LaRosa, H. D. Hallen, and M. A. Paesler, "Thermal/optical effects in NSOM probes," *Ultramicroscopy*, vol. 61, pp. 179-185, Dec 1995.

[16] C. Lienau, A. Richter, and T. Elsaesser, "Light-induced expansion of fiber tips in near-field scanning optical microscopy," *Applied Physics Letters*, vol. 69, pp. 325-327, Jul 15 1996.

[17] P. G. Gucciardi, M. Colocci, M. Labardi, and M. Allegrini, "Thermal-expansion effects in near-field optical microscopy fiber probes induced by laser light absorption," *Applied Physics Letters*, vol. 75, pp. 3408-3410, Nov 22 1999.

[18] D. Kazantsev, G. Guttroff, M. Bayer, and A. Forchel, "Sample temperature measurement in a scanning near-field optical microscope," *Applied Physics Letters,* vol. 72, pp. 689-691, Feb 9 1998.

[19] A. H. La Rosa and H. D. Hallen, "Compact method for optical induction of proximal probe heating and elongation," *Applied Optics,* vol. 41, pp. 2015-2019, Apr 1 2002.

[20] P. G. Gucciardi, S. Patane, A. Ambrosio, M. Allegrini, A. D. Downes, G. Latini, *et al.,* "Observation of tip-to-sample heat transfer in near-field optical microscopy using metal-coated fiber probes," *Applied Physics Letters,* vol. 86, May 16 2005.

[21] A. Ambrosio, O. Fenwick, F. Cacialli, R. Micheletto, Y. Kawakami, P. G. Gucciardi, *et al.,* "Shape dependent thermal effects in apertured fiber probes for scanning near-field optical microscopy," *Journal of Applied Physics,* vol. 99, Apr 15 2006.

[22] N. E. Dickenson, E. S. Erickson, O. L. Mooren, and R. C. Dunn, "Characterization of power induced heating and damage in fiber optic probes for near-field scanning optical microscopy," *Review of Scientific Instruments,* vol. 78, May 2007.

[23] W. J. Chang, H. L. Lee, Y. C. Yang, and S. S. Chu, "Vibration of scanning near-field optical microscope probe with laser-induced thermal effect using Timoshenko beam theory," *Applied Physics B-Lasers and Optics,* vol. 97, pp. 653-659, Nov 2009.

[24] A. Soni, V. M. Sundaram, and S. B. Wen, "The generation of nano-patterns on a pure silicon wafer in air and argon with sub-diffraction limit nanosecond laser pulses," *Journal of Physics D-Applied Physics,* vol. 43, Apr 14 2010.

[25] V. M. Sundaram, A. Soni, R. E. Russo, and S. B. Wen, "Analysis of nanopatterning through near field effects with femtosecond and nanosecond lasers on semiconducting and metallic targets," *Journal of Applied Physics,* vol. 107, Apr 1 2010.

[26] S. B. Wen, "Optical and thermal energy transport from a NSOM probe to a pure silicon target under intense ns pulsed light," *Journal of Physics D-Applied Physics,* vol. 43, Jul 21 2010.

[27] M. Stahelin, M. A. Bopp, G. Tarrach, A. J. Meixner, and I. ZschokkeGranacher, "Temperature profile of fiber tips used in scanning near-field optical microscopy," *Applied Physics Letters,* vol. 68, pp. 2603-2605, May 6 1996.

[28] D. I. Kavaldjiev, R. Toledocrow, and M. Vaeziravani, "On the Heating of the Fiber Tip in a near-Field Scanning Optical Microscope," *Applied Physics Letters,* vol. 67, pp. 2771-2773, Nov 6 1995.

[29] E. Hecht, *Optics*, 4th ed. Reading, Mass.: Addison-Wesley, 2002.

[30] R. J. Potton, "Reciprocity in optics," *Reports on Progress in Physics,* vol. 67, pp. 717-754, May 2004.

[31] R. Zenobi, R. M. Stockle, N. Schaller, V. Deckert, and C. Fokas, "Brighter near-field optical probes by means of improving the optical destruction threshold," *Journal of Microscopy-Oxford,* vol. 194, pp. 378-382, May-Jun 1999.

[32] R. Zenobi, L. Zhu, G. Gamez, T. A. Schmitz, and F. Krumeich, "Material ejection and redeposition following atmospheric pressure near-field laser ablation on molecular solids," *Analytical and Bioanalytical Chemistry*, vol. 396, pp. 163-172, Jan 2010.

[33] W. X. Sun and Z. X. Shen, "Optimizing the near field around silver tips," *Journal of the Optical Society of America a-Optics Image Science and Vision*, vol. 20, pp. 2254-2259, Dec 2003.

[34] O. J. F. Martin, C. Girard, and A. Dereux, "Generalized Field Propagator for Electromagnetic Scattering and Light Confinement," *Physical Review Letters*, vol. 74, pp. 526-529, Jan 23 1995.

[35] L. Novotny, D. W. Pohl, and B. Hecht, "Light confinement in scanning near-field optical microscopy," *Ultramicroscopy*, vol. 61, pp. 1-9, Dec 1995.

[36] Y. C. Martin, H. F. Hamann, and H. K. Wickramasinghe, "Strength of the electric field in apertureless near-field optical microscopy," *Journal of Applied Physics*, vol. 89, pp. 5774-5778, May 15 2001.

[37] L. Liu and S. L. He, "Design of metal-cladded near-field fiber probes with a dispersive body-of-revolution finite-difference time-domain method," *Applied Optics*, vol. 44, pp. 3429-3437, Jun 10 2005.

[38] S. B. Wen and R. Greif, "Combined wave based optical analysis and particle based thermal analysis of nanoscale ultrafast target heating of silicon utilizing a near-field scanning optical probe and a femtosecond laser," *Journal of Physics D-Applied Physics*, vol. 42, Apr 7 2009.

[39] G. Chen, "Nanoscale heat transfer and nanostructured thermoelectrics," *Ieee Transactions on Components and Packaging Technologies,* vol. 29, pp. 238-246, Jun 2006.

[40] R. S. Timsit, "Comment on "Abnormal contact resistance reduction of bonded copper interconnects in three-dimensional integration during current stressing"," *Applied Physics Letters,* vol. 88, Feb 6 2006.

[41] B. Dutoit, D. Zeisel, V. Deckert, and R. Zenobi, "Laser-induced ablation through nanometer-sized tip apertures: Mechanistic aspects," *Journal of Physical Chemistry B,* vol. 101, pp. 6955-6959, Aug 28 1997.

[42] B. Hecht, B. Sick, U. P. Wild, V. Deckert, R. Zenobi, O. J. F. Martin, *et al.*, "Scanning near-field optical microscopy with aperture probes: Fundamentals and applications," *Journal of Chemical Physics,* vol. 112, pp. 7761-7774, May 8 2000.

[43] S. Nolte, B. N. Chichkov, H. Welling, Y. Shani, K. Lieberman, and H. Terkel, "Nanostructuring with spatially localized femtosecond laser pulses," *Optics Letters,* vol. 24, pp. 914-916, Jul 1 1999.

[44] D. J. Hwang, A. Chimmalgi, and C. P. Grigoropoulos, "Ablation of thin metal films by short-pulsed lasers coupled through near-field scanning optical microscopy probes," *Journal of Applied Physics,* vol. 99, Feb 15 2006.

[45] D. J. Hwang, C. P. Grigoropoulos, J. Yoo, and R. E. Russo, "Optical near-field ablation-induced plasma characteristics," *Applied Physics Letters,* vol. 89, Dec 18 2006.

[46] D. J. Hwang, H. Jeon, and C. P. Grigoropoulos, "Laser ablation-induced plasma characteristics in optical near-field," *Proceedings of the Asme/Jsme Thermal Engineering Summer Heat Transfer Conference 2007, Vol 2,* pp. 357-364, 2007.

[47] D. J. Hwang, H. Jeon, C. P. Grigoropoulos, J. Yoo, and R. E. Russo, "Laser ablation-induced spectral plasma characteristics in optical far- and near fields," *Journal of Applied Physics,* vol. 104, Jul 1 2008.

[48] S. B. Wen, R. Greif, and R. E. Russo, "Background gas effects on the generation of nanopatterns on a pure silicon wafer with multiple femtosecond near field laser ablation," *Applied Physics Letters,* vol. 91, Dec 17 2007.

[49] V. Zorba, X. L. Mao, and R. E. Russo, "Optical far- and near-field femtosecond laser ablation of Si for nanoscale chemical analysis," *Analytical and Bioanalytical Chemistry,* vol. 396, pp. 173-180, Jan 2010.

[50] A. Soni, V. Sundaram, and S. B. Wen, "Generation of nano-patterns on a pure silicon wafer in air and pure argon with sub-diffraction limit nanosecond laser pulses," *Applied Physics Letters,* vol. Submitting.

[51] L. Novotny and B. Hecht, "Principles of Nano-Optics," *Cambridge University Press, Cambridge,* 2006.

[52] S. B. Wen, "Optical and thermal energy transport from a NSOM probe to a pure silicon target under intense ns pulsed light " *Journal of Applied Physics,* submitting.

[53] J. P. Girardeau-Montaut and C. Girardeau-Montaut, "Theory of ultrashort nonlinear multiphoton photoelectric emission from metals," *Physical Review B,* vol. 51, p. 13560, 1995.

[54] V. Sundaram and S. B. Wen, "Characteristics of nanopatterns and the associated thermal mechanisms during near field laser-material interaction of nanosecond laser on different targets," *ASME* vol. HT2009-88225, July 19-23, 2009 2009.

[55] S. B. Wen, R. Greif, and R. E. Russo, "Background gas effects on the generation of nanopatterns on a pure silicon wafer with multiple femtosecond near field laser ablation," *Applied Physics Letters,* vol. 91, pp. -, Dec 17 2007.

[56] N. Birks, G. H. Meier, and F. S. Pettit, "Introduction to the High Temperature Oxidation of Metals," *Cambridge University Press, Cambridge,* 2006.

[57] G. Latini, A. Downes, O. Fenwick, A. Ambrosio, M. Allegrini, C. Daniel, *et al.*, "Optical probing of sample heating in scanning near-field experiments with apertured probes," *Applied Physics Letters,* vol. 86, Jan 3 2005.

[58] H. D. Hallen, B. I. Yakobson, A. Larosa, and M. A. Paesler, "Thermal temporal response of the NSOM probe sample system," *Near-Field Optics,* vol. 2535, pp. 34-37, 1995.

[59] A. Ambrosio, M. Allegrini, G. Latini, and F. Cacialli, "Thermal processes in metal-coated fiber probes for near-field experiments," *Applied Physics Letters,* vol. 87, Jul 18 2005.

[60] H. L. Lee, W. J. Chang, W. L. Chen, and Y. C. Yang, "An inverse problem of estimating the heat source in tapered optical fibers for scanning near-field optical microscopy," *Ultramicroscopy,* vol. 107, pp. 656-662, Aug 2007.

[61] M. Farzaneh, K. Maize, D. Luerssen, J. A. Summers, P. M. Mayer, P. E. Raad, *et al.*, "CCD-based thermoreflectance microscopy: principles and applications," *Journal of Physics D-Applied Physics,* vol. 42, Jul 21 2009.

[62] S. Grauby, S. Dilhaire, S. Jorez, and W. Claeys, "Imaging setup for temperature, topography, and surface displacement measurements of microelectronic devices," *Review of Scientific Instruments,* vol. 74, pp. 645-647, Jan 2003.

[63] S. Dilhaire, S. Grauby, and W. Claeys, "Calibration procedure for temperature measurements by thermoreflectance under high magnification conditions," *Applied Physics Letters,* vol. 84, pp. 822-824, Feb 2 2004.

[64] M. G. Burzo, P. L. Komarov, and P. E. Raad, "Optimized thermo-reflectance system for measuring the thermal properties of thin-films and their interfaces," *Twenty Second Annual IEEE Semiconductor Thermal Measurement and Management Symposium, Proceedings 2006,* pp. 87-94, 2006.

[65] B. Vermeersch, J. Christofferson, K. Maize, A. Shakouri, and G. De Mey, "Time and Frequency Domain CCD-Based Thermoreflectance Techniques for High-Resolution Transient Thermal Imaging," *26th Annual Ieee Semiconductor Thermal Measurement and Management Symposium, Proceedings 2010,* pp. 228-234, 2010.

[66] A. Soni and S. B. Wen, "Non-intrusive temperature measurement of NSOM probes with thermoreflectance imaging," *Journal of Physics D-Applied Physics,* vol. 45, May 9 2012.

[67] D. Luerssen, J. A. Hudgings, P. M. Mayer, and R. J. Ram, "Nanoscale thermoreflectance with 10mK temperature resolution using stochastic resonance," *Twenty-First Annual IEEE Semiconductor Thermal Measurement and Management Symposium, Proceedings 2005,* pp. 253-258, 2005.

[68] P. M. Mayer, D. Luerssen, R. J. Ram, and J. A. Hudgings, "Theoretical and experimental investigation of the thermal resolution and dynamic range of CCD-based thermoreflectance imaging," *Journal of the Optical Society of America a-Optics Image Science and Vision,* vol. 24, pp. 1156-1163, Apr 2007.

[69] G. Tessier, S. Hole, and D. Fournier, "Quantitative thermal imaging by synchronous thermoreflectance with optimized illumination wavelengths," *Applied Physics Letters,* vol. 78, pp. 2267-2269, Apr 15 2001.

[70] A. L. Mattheyses, K. Shaw, and D. Axelrod, "Effective elimination of laser interference fringing in fluorescence microscopy by spinning azimuthal incidence angle," *Microscopy Research and Technique,* vol. 69, pp. 642-647, Aug 2006.

[71] R. Thariani and P. Yager, "Novel, high-quality surface plasmon resonance microscopy," *Sensors and Actuators B-Chemical,* vol. 130, pp. 765-770, Mar 28 2008.

[72] M. N. Akram, Z. M. Tong, G. M. Ouyang, X. Y. Chen, and V. Kartashov, "Laser speckle reduction due to spatial and angular diversity introduced by fast scanning micromirror," *Applied Optics*, vol. 49, pp. 3297-3304, Jun 10 2010.

[73] M. N. Özışık, *Basic heat transfer*. Malabar, Fla.: R.E. Krieger Pub. Co., 1987.

[74] E. D. Palik, "Handbook of Optical-Constants," *Journal of the Optical Society of America a-Optics Image Science and Vision*, vol. 1, pp. 1297-1297, 1984.

[75] Y. Ezzahri, J. Christofferson, G. Zeng, and A. Shakouri, "Short time transient thermal behavior of solid-state microrefrigerators," *Journal of Applied Physics*, vol. 106, Dec 1 2009.

[76] V. Moreau, G. Tessier, F. Raineri, M. Brunstein, A. Yacomotti, R. Raj, *et al.*, "Transient thermoreflectance imaging of active photonic crystals," *Applied Physics Letters*, vol. 96, Mar 1 2010.

[77] J. Christofferson, K. Yazawa, and A. Shakouri, "Picosecond Transient Thermal Imaging Using a Ccd Based Thermoreflectance System," *Proceedings of the Asme International Heat Transfer Conference - 2010, Vol 4*, pp. 93-97, 2010.

[78] J. W. Goodman, *Speckle phenomena in optics : theory and applications*. Englewood, Colo.: Roberts & Co., 2007.

[79] E. Wolf, *Introduction to the theory of coherence and polarization of light*. Cambridge: Cambridge University Press, 2007.

[80] J. I. Trisnadi, "Speckle contrast reduction in laser projection displays," *Projection Displays Viii*, vol. 4657, pp. 131-137, 2002.

[81] D. Kohler, W. L. Seitz, T. R. Loree, and S. D. Gardner, "Speckle Reduction in Pulsed-Laser Photographs," *Optics Communications*, vol. 12, pp. 24-28, 1974.

[82] J. G. Manni and J. W. Goodman, "Versatile method for achieving 1% speckle contrast in large-venue laser projection displays using a stationary multimode optical fiber," *Optics Express*, vol. 20, pp. 11288-11315, May 7 2012.

[83] G. Chen, *Nanoscale energy transport and conversion : a parallel treatment of electrons, molecules, phonons, and photons*. New York: Oxford University Press, 2005.